

HaloFlow II: Robust Galaxy Halo Mass Inference with Domain Adaptation

NIKHIL GARUDA,^{1,2} CHANGHOON HAHN,^{1,2} CONNOR BOTTRELL,³ AND KHEE-GAN LEE^{4,5}

¹*Department of Astronomy, The University of Texas at Austin, 2515 Speedway Boulevard, Austin, TX 78712, USA*

²*Cosmic Frontier Center, The University of Texas at Austin, Austin, TX, USA**

³*International Centre for Radio Astronomy Research, University of Western Australia, 35 Stirling Hwy, Crawley, WA 6009, Australia*

⁴*Kavli IPMU (WPI), UTIAS, The University of Tokyo, Kashiwa, Chiba 277-8583, Japan*

⁵*Center for Data-Driven Discovery, Kavli IPMU (WPI), UTIAS, The University of Tokyo, Kashiwa, Chiba 277-8583, Japan*

ABSTRACT

Precise halo mass (M_h) measurements are crucial for cosmology and galaxy formation. HaloFlow (C. Hahn et al. 2024) introduced a simulation-based inference (SBI) framework that uses state-of-the-art simulated galaxy images to precisely infer M_h . However, for HaloFlow to be applied to observations, it must be generalizable even when the underlying galaxy formation physics differ from those in the simulations on which it was trained. Without this generalization, HaloFlow produces biased and overconfident M_h posteriors when applied to simulations with different physics. We introduce HaloFlow^{DA}, an extension of HaloFlow that integrates domain adaptation (DA) with SBI to mitigate these cross-simulation shifts. Using synthetic galaxy images forward-modeled from the IllustrisTNG, EAGLE, and SIMBA simulations, we test two DA methods: Domain-Adversarial Neural Networks (DANN) and Maximum Mean Discrepancy (MMD). Incorporating DA significantly reduces bias and improves calibration, with MMD achieving the most stable performance, lowering the normalized residual metric, β , by an average of 31% and up to 57% when trained and tested on different simulations. Overall, HaloFlow^{DA} produces more robust, less biased with similar precision, M_h constraints than the standard approach using the stellar-to-halo mass relation. HaloFlow^{DA} enables consistent, simulation-trained inference models to generalize across domains, establishing a foundation for robust M_h inference from real HSC-SSP observations.

1. INTRODUCTION

Robustly inferring the host dark matter halo masses of galaxies plays a critical role in cosmology and galaxy evolution studies. The most massive halos that host galaxy clusters are promising probes of the expansion history of the Universe and the growth rate of structure (*e.g.*, A. Albrecht et al. 2006). Host halos also play a major role in the evolution of galaxies (*e.g.*, R. H. Wechsler & J. L. Tinker 2018), with halo mass playing the most dominant role in the galaxy-halo connection (*e.g.*, J. Tinker et al. 2011; P. Behroozi et al. 2019). Halo masses are also crucial for studying cosmic baryon distribution using fast radio bursts (FRBs; K.-G. Lee et al. 2022; K.-G. Lee et al. 2023), which probe the amount and extent of circumgalactic medium (CGM). Interpreting these FRB-based CGM measurements relies on the baryon-dark matter scaling relations, which quantify how baryon content varies with dark matter

halo mass (M. Ayromlou et al. 2023; A. Sullivan et al. 2024), enabling constraints on the total baryon fraction in halos.

Despite its importance, the halo mass of an individual galaxy is not directly observable. Traditional approaches, therefore, rely on indirect methods. Weak and strong gravitational lensing provide relatively direct constraints on projected mass profiles, but high-fidelity measurements require deep, high-resolution imaging and large background source densities (T. Treu 2010; H. Hoekstra et al. 2013; M. Bartelmann & M. Maturi 2016; R. Mandelbaum 2018; A. J. Shajib et al. 2024; P. Natarajan et al. 2024). These requirements make lensing observationally expensive, limit its applicability to low-mass halos (S.-S. Li et al. 2025), and can restrict analyses to stacked measurements over ensembles of galaxies rather than precise constraints for individual systems (R. d. Putter & M. White 2005; X. Yang et al. 2006).

A complementary set of techniques infers halo masses statistically from galaxy properties. Abundance-matching techniques relate galaxies to dark matter ha-

Email: garuda@utexas.edu

* galactic.ai

los by requiring consistency between observed luminosity or stellar-mass functions and the halo mass function (A. V. Kravtsov et al. 2004; A. Tasitsiomi et al. 2004; A. Vale & J. P. Ostriker 2004; A. P. Hearin et al. 2013; B. P. Moster et al. 2013). While these methods have been highly successful in recovering the average stellar-to-halo mass relation and its scatter (D. Zaritsky & P. Behroozi 2022), they constrain halo mass applied to an aggregated ensemble of galaxies.

A distinct class of approaches estimates halo masses of galaxy groups or clusters by leveraging group dynamics, especially in large spectroscopic surveys (V. R. Eke et al. 2004; X. Yang et al. 2007, 2009; A. S. G. Robotham et al. 2011; R. Wojtak et al. 2018). In these methods, group-finding algorithms are used to identify associations of galaxies, after which dynamical masses are estimated using the measured velocity dispersion and projected radius of group members through application of the virial theorem or related mass estimators (J. Heisler et al. 1985; T. C. Beers et al. 1990; A. S. G. Robotham et al. 2011; J. Tinker et al. 2011; J. L. Tinker 2022; T. S. Lambert et al. 2026). These methods provide valuable, often direct, constraints on halo mass; however, they are not designed to deliver well-calibrated posterior distributions of halo mass for individual galaxies.

The rapid growth of wide, deep imaging surveys and realistic cosmological simulations has opened a complementary path: using machine learning (ML) to learn the mapping between galaxy observables and halo properties directly (M. Ntampaka et al. 2015, 2016; V. F. Calderon & A. A. Berlind 2019; P. Villanueva-Domingo et al. 2022; J. F. Wu et al. 2024; N. Garuda et al. 2024). In particular, simulation-based inference (SBI; see K. Cranmer et al. 2020, for recent review) denotes a broad class of likelihood-free methods that use forward models to generate mock observations. Among the various SBI approaches, we focus on those based on neural density estimation, in which flexible conditional density models are trained on simulated data. In the variant known as neural posterior estimation (NPE; G. Papamakarios & I. Murray 2018; D. S. Greenberg et al. 2019), these networks directly approximate the posterior distribution of the parameters given the observations, $p(\theta | \mathbf{X})$.

HaLoFlow (C. Hahn et al. 2024) uses NPE with normalising flows (E. G. Tabak & E. Vanden-Eijnden 2010; E. G. Tabak & C. V. Turner 2013) to infer the joint posterior of stellar and halo mass from photometric, morphological, and structural features extracted from synthetic galaxy images. C. Hahn et al. (2024) demonstrated that HaLoFlow can recover accurate and well-calibrated posteriors when trained and tested on galaxies drawn from the same cosmological hydrody-

namical simulation. Moreover, it demonstrated that we can derive more precise M_h constraints by leveraging imaging features beyond photometry.

However, like most ML approaches, HaLoFlow inherits a key limitation: it is intrinsically dataset-specific. In practice, the network learns the mapping between features \mathbf{X} and parameters θ implied by the training simulation, and implicitly assumes that the data it is applied to are drawn from the same underlying generative process (in-domain). This assumption is violated as soon as we move beyond the idealized “train and test on the same simulation” case. When a model trained on one simulation is applied either to a different simulation or, ultimately, to real observations, the mapping between \mathbf{X} and θ encoded by the inference pipeline no longer matches the true generative process (out-of-domain). Each simulation we consider has different physical models of galaxy formation. None is precisely accurate to the physics of the *real* Universe. This kind of domain shift constitutes model misspecification (P. Cannon et al. 2022; D. Huang et al. 2023; N. A. Montel et al. 2025). As we show later in this work, such shifts can drive HaLoFlow to produce biased and over-confident posteriors for M_h .

To mitigate these effects, we seek techniques that enable an NPE trained on one to make reliable inferences in another. A common strategy is to modify the internal features learned by the network so that they become less sensitive to the choice of domain, while still retaining the information needed for precise inference. Unsupervised domain adaptation (DA; W. M. Kouw & M. Loog 2019; A. Farahani et al. 2020) provides a natural framework for this problem. In DA, one has labeled data in one or more source domains and unlabeled data in a target domain. The goal is to learn some feature representation of the data in which the distributions of training and test representations are statistically aligned, while preserving the information needed for the primary task. A variety of DA strategies have been developed, including adversarial methods such as Domain-Adversarial Neural Networks (DANN; Y. Ganin et al. 2017) and distance-based approaches that minimize measures like the maximum mean discrepancy (MMD; A. Gretton et al. 2008) between feature distributions. DA has already seen successful applications in astronomy and cosmology, for example, in galaxy morphology classification (A. Ćiprijanović et al. 2022, 2023), supernova classification (R. Vilalta et al. 2019), cosmological parameter inference (A. Roncoli et al. 2024), and strong-lensing detection (H. Parul et al. 2025) and parameter estimation (P. Swierc et al. 2023; S. Agarwal et al. 2025).

In this work we bring DA into the `HaLoFlow` framework to improve the robustness of M_h inference under domain shifts. We use forward-modeled galaxy images from state-of-the-art cosmological hydrodynamical simulations: `IllustrisTNG` (D. Nelson et al. 2019a), `EAGLE` (J. Schaye et al. 2015), and `SIMBA` (R. Davé et al. 2019)–processed with radiative-transfer and survey-realism pipelines (C. Bottrell et al. 2024; L. Eisert et al. 2024) to mimic Hyper Suprime-Cam Subaru Strategic Program (HSC-SSP; H. Aihara et al. 2022) observations. We treat each simulation as a distinct domain and explicitly quantify how `HaLoFlow`’s performance degrades when trained on one simulation and evaluated on another. We then introduce `HaLoFlow`^{DA}, a domain-adapted extension of `HaLoFlow` in which an intermediate DA network maps observed features \mathbf{X} into compressed, domain-invariant representations $c\mathbf{X}$ that are subsequently used as input to the NPE. By construction, these representations are encouraged to discard simulation-specific features while retaining information relevant for M_h . Although our ultimate goal is to apply `HaLoFlow`^{DA} to real survey data, in this paper we use multiple simulations as controlled proxies for the unknown mismatch between any given simulation and the real Universe, and we demonstrate that `HaLoFlow`^{DA} substantially improves out-of-domain performance.

We begin in §2 with a brief description of the hydrodynamical simulations and the forward-modeled synthetic images. In §3, we present `HaLoFlow`, introduce the two DA techniques (DANN and MMD), and define `HaLoFlow`^{DA}, which combines `HaLoFlow` with domain adaptation. We then present the results of applying `HaLoFlow`^{DA} in §4, discuss their implications in §5, and conclude in §6.

2. DATA

The main goal of this work is to enable robust SBI of M_* and M_h from galaxy images. Achieving this requires realistic synthetic observations that incorporate both galaxy formation physics and observational systematics. To this end, we use forward-modeled galaxy images from state-of-the-art cosmological hydrodynamical simulations. Furthermore, we want to demonstrate that `HaLoFlow`^{DA} is robust to domain shift so that we can ultimately apply it to observations. Therefore, we use simulations that adopt different sets of subgrid prescriptions, galaxy formation physics, and resolution.

2.1. Cosmological Hydrodynamical Simulations

We use four large-scale cosmological hydrodynamical simulations as the basis for generating forward-modeled galaxy images: `TNG50` and `TNG100` from the `Illus-`

`trisTNG` suite, `EAGLE Ref-L100N1504`, and `SIMBA m100n1024`.

`IllustrisTNG` utilizes the moving-mesh magnetohydrodynamics code `AREPO` (V. Springel 2010). We use `TNG50` (D. Nelson et al. 2019b; A. Pillepich et al. 2019) and `TNG100` (V. Springel et al. 2018; A. Pillepich et al. 2018; J. P. Naiman et al. 2018; D. Nelson et al. 2018; F. Marinacci et al. 2018), which span $(51.7 \text{ Mpc})^3$ and $(110.7 \text{ Mpc})^3$ volumes respectively. `TNG50` has high spatial and mass resolution (baryon mass resolution of $M_b \sim 8.5 \times 10^4 M_\odot$) capable of resolving detailed internal galaxy structure, while `TNG100` samples a larger volume at a coarser resolution ($M_b \sim 1.4 \times 10^6 M_\odot$). Both runs adopt the same subgrid galaxy-formation model, including two-mode AGN feedback (thermal and kinetic) and kinetic stellar winds, although some subgrid parameter values are adjusted between `TNG50` and `TNG100` to account for the different resolution.

To leverage the strengths of both volumes, we combine the `TNG50` and `TNG100` datasets by applying systematic corrections to the `TNG50` galaxy properties. Specifically, stellar masses in `TNG50` are adjusted by aligning the stellar-halo mass relation (SHMR) with that of `TNG100` over well-sampled mass ranges, following the mass-modulated rescaling procedure described in Appendix A1 of A. Pillepich et al. (2018)⁶. Magnitudes and surface brightnesses are similarly corrected by applying the same magnitude corrections to Sersic magnitudes and related parameters. These corrections are derived from boxcar-averaged offsets between `TNG50` and `TNG100` as a function of halo mass, enabling smooth interpolation. This calibration step ensures that the combined TNG dataset presents a physically consistent distribution of galaxy properties.

`EAGLE` (J. Schaye et al. 2015; R. A. Crain et al. 2015) uses a modified smoothed particle hydrodynamics code, `GADGET-3`, with the “Anarchy” hydrodynamics scheme (M. Schaller et al. 2015). We use the `Ref-L100N1504` run with a $(100 \text{ Mpc})^3$ volume and 1504^3 particles per species ($M_b \sim 1.8 \times 10^6 M_\odot$). `EAGLE` employs stochastic thermal stellar and AGN feedback, with subgrid parameters calibrated primarily to reproduce the $z \approx 0.1$ galaxy stellar mass function, galaxy sizes, and the black hole mass–stellar mass relation (R. A. Crain et al. 2015).

`SIMBA` is built on the `GIZMO` (P. F. Hopkins 2015, 2017) code in meshless finite mass mode (R. Davé et al.

⁶ This approach corrects for resolution-dependent discrepancies by applying a smooth, halo-mass-dependent correction, derived from the ratio of SHMRs between the two simulations, to the `TNG50` stellar masses.

2019). We use the flagship m100n1024 run, a $(100 h^{-1} \text{ Mpc})^3$ volume with 1024^3 particles per species ($M_b \sim 1.8 \times 10^7 M_\odot$). SIMBA incorporates an H_2 -based star formation model, kinetic stellar winds, and a multi-mode AGN feedback scheme with high-velocity jets and X-ray heating, leading to distinct gas and halo properties compared to TNG and EAGLE.

In this work, we focus exclusively on central galaxies at redshift $z = 0.1$ and $M_* > 10^{10} M_\odot$, selected from each simulation using the Friends-of-Friends (FoF) group catalogs. Central galaxies are identified as the primary subhalo within each FoF group, determined using the SUBFIND algorithm (V. Springel et al. 2001). For each central galaxy, we extract its M_* and host M_h from the simulation outputs.

2.2. Realistic Synthetic Images

We use publicly released synthetic galaxy images⁷ from the simulations described above. These images are produced with the forward-model described in C. Bottrell et al. (2024), adapted to work across multiple cosmological simulation suites (L. Eisert et al. 2024). This forward-model yields realistic, observation-like data for use in SBI. The image-generation workflow comprises two stages: (1) dust-attenuated, noise-free rendering with SKIRT, and (2) observational realism that injects simulated galaxy light into HSC cutouts.

In this framework, noise-free synthetic images are generated using the SKIRT dust radiative transfer code⁸ (M. Baes et al. 2011; P. Camps & M. Baes 2015, 2020). For each central galaxy at $z = 0.1$, star and gas particle data are extracted within a spherical volume centered on the galaxy’s FoF halo, capturing its physical and environmental context. The radiative transfer simulation computes the propagation of starlight through a dusty medium, accounting for absorption, scattering, and thermal re-emission.

Idealized synthetic images in the HSC *grizy* bands (S. Kawanomoto et al. 2018) are produced, along with several auxiliary filters spanning $0.3\text{--}5 \mu\text{m}$. To account for orientation-dependent effects and enhance the diversity of the dataset, each galaxy is rendered along four lines of sight, arranged in a tetrahedral configuration.

Stellar emission is modeled using the G. Bruzual & S. Charlot (2003) stellar population synthesis templates with a G. Chabrier (2003) initial mass function (IMF) for stars older than 10 Myr. For younger stellar populations (< 10 Myr), the MAPPINGS III SED library (B. Groves et al. 2008) is adopted, which includes nebular

Table 1. Observational features (\mathbf{X}) of galaxy images used to infer M_* and M_h in `Haloflow`^{DA}

Observations	Parameters
X_{mag}	HSC <i>grizy</i> magnitudes
X_{morph}	$R_{\text{eff}}, n, b/a$
X_{extra}	$CAS, G, M_{20}, \mu_{1 \text{ kpc}}, A_{\text{res}}$

emission, dust continuum, and line emission from H II regions and photodissociation regions.

Dust is modeled using a metallicity-scaled dust-to-gas prescription based on A. Rémy-Ruyer et al. (2014) and G. Popping et al. (2022), assuming a Milky Way dust grain size distribution and composition. While only some simulations (*e.g.*, SIMBA) explicitly track dust particles, this ensures a uniform and realistic attenuation treatment across all simulations.

To emulate observational conditions, the survey systematics of the HSC-SSP Public Data Release 3 (H. Aihara et al. 2022) are applied to the noise-free synthetic images. Using an adapted version of `RealSim`⁹ (C. Bottrell et al. 2019), simulated galaxy images are inserted into real HSC background cutouts, with realistic point spread functions, spatial rebinning, pixel-level blending, and flux calibration applied. The resulting HSC-like mock images statistically reflect the depth, seeing, and crowding of real galaxy survey data.

Figure 1 shows HSC mock images for randomly selected galaxies at $z = 0.1$ from EAGLE, SIMBA, TNG100, and TNG50 (left to right) with increasing stellar mass (top to bottom). These images illustrate the morphological diversity predicted by each simulation suite with consistent observational realism.

Photometric and morphological features are extracted using `ProFuse` (A. S. G. Robotham et al. 2022). Source identification and segmentation are performed with `ProFound` (A. S. G. Robotham et al. 2018) on a *grizy* stacked image, after which `ProFit` (A. S. G. Robotham et al. 2017) is used to fit a single-component Sérsic profile to the target galaxy independently in each band. We additionally measure a suite of non-parametric morphology statistics. These measurements form the observational data vector \mathbf{X} used in SBI. The data vector \mathbf{X} is the combination of $X_{\text{mag}} + X_{\text{morph}} + X_{\text{extra}}$.

HSC *grizy* magnitudes come from `ProFound` photometry. R_{eff} and n and b/a are the Sérsic effective radius, characteristic index, and semi minor-to-major axis ratio. *CAS* parameters are concentration, asymmetry, and smoothness (C. J. Conselice 2003). G is the Gini

⁷ <https://www.tng-project.org/explore/gallery/bottrell23/>

⁸ <https://skirt.ugent.be/>

⁹ <https://github.com/cbottrell/RealSim>

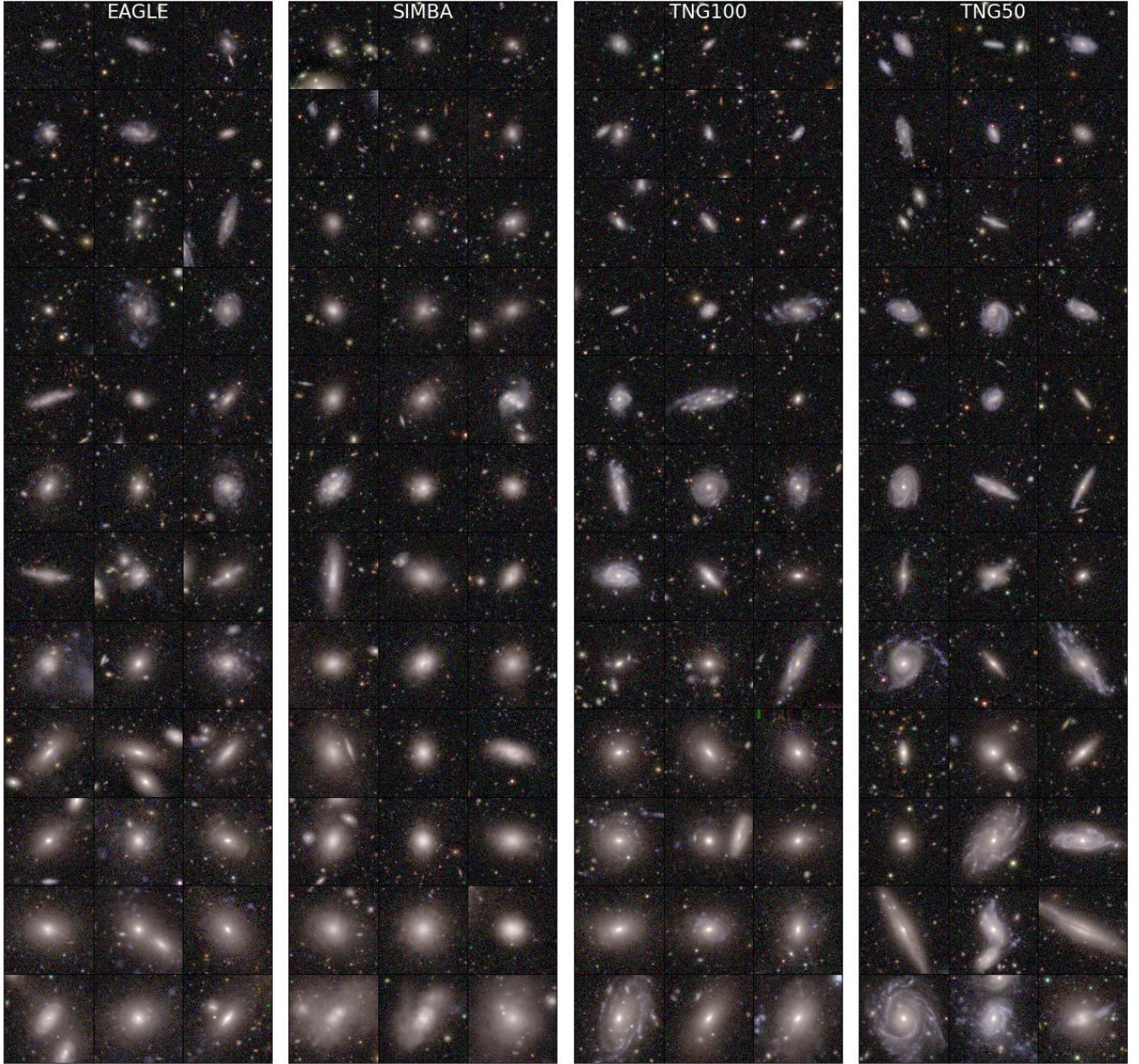


Figure 1. HSC mock images of simulated galaxies from the $z \approx 0.1$ snapshot of EAGLE, SIMBA, TNG100, and TNG50 (left to right) simulations. 36 central galaxies with stellar masses $10 < \log(M_*/M_\odot) < 11.6$ are shown. Stellar masses increase from upper to lower rows. Individual panels are 120 kpc (63 arcsec) across. RGB colours derive from the HSC *gri* optical bands using arcsinh scaling.

coefficient and M_{20} is the second-order moment of the brightest pixels containing 20 percent of the galaxy flux (J. M. Lotz et al. 2004). $\mu_{1 \text{ kpc}}$ is the mean surface brightness within 1kpc of the galaxy centre, A_{res} is residual asymmetry (L. Simard et al. 2011). The observation features are listed in Table 1. We note that for our purposes of demonstrating $\text{HaloFlow}^{\text{DA}}$, we do not include the total measured luminosity, L_{sat} , and number, N_{sat} , of satellites brighter than $M_r < -18$ for each

individual group, which were included in the previous HaloFlow work.

The final dataset with four line of sight per galaxy includes 2,136 galaxies from TNG50 and 15,364 from TNG100 (total 17,500 for TNG), along with 8,888 galaxies from EAGLE and 8,831 from SIMBA. The dataset is divided into training and testing sets using a 90-10 split.

3. METHODS

In this section, we describe our methodology for inferring M_h from galaxy observations using SBI. Specifically, we describe how we incorporate DA into the `Haloflow` framework. SBI methods like `Haloflow` can recover accurate M_h posteriors in in-domain settings, where training and test data are drawn from the same simulation. In such cases, the NPE encodes a specific galaxy-formation model and set of physical and numerical assumptions that are consistent across train and test samples. This assumption often breaks down in out-of-domain scenarios, where there is a domain shift between the training and test samples (*e.g.*, TNG \Rightarrow EAGLE).

To address this, we introduce DA as an intermediate step before performing SBI. DA techniques aim to reduce differences across training and test domains — in this case, across simulations with different galaxy formation physics — to improve generalisation and enable more robust inference. We first train a DA network to map the observational features \mathbf{X} into compressed, domain-invariant representations $c\mathbf{X}$, and then use $c\mathbf{X}$ as input to the `Haloflow` SBI framework to learn $p(M_*, M_h | c\mathbf{X})$.

In this work, we use the different simulations as training and test domains. That is, we treat different cosmological simulations (TNG, EAGLE, SIMBA) as distinct domains and use them as a controlled testbed to study the impact of DA. Our working hypothesis is that techniques which improve generalization across simulations will also improve generalization to observational data. We refer to our domain-adaptive SBI framework as `Haloflow`^{DA}. In the subsections that follow, we detail its components: the SBI framework (§3.1) and our DA strategy (§3.2).

3.1. *Haloflow*

`Haloflow` is a SBI framework used to infer the posterior $p(\theta | \mathbf{X})$ where $\theta = \{M_*, M_h\}$ represents stellar and halo mass, and \mathbf{X} denotes a set of features extracted from synthetic galaxy images. SBI¹⁰, enables posterior inference without requiring an explicit likelihood function. Instead, it leverages forward simulations that generate synthetic data \mathbf{X} conditioned on physical parameters θ . These forward models implicitly define the likelihood by simulating the data generation process from physical parameters to observable features.

`Haloflow` is based on NPE using “normalising flow” models. Flows use neural networks that maps complex

target distributions to a simple base distribution, $\pi(z)$ via a sequence of invertible and bijective transformations, $f : x \rightarrow z$. The target distribution here is the posteriors $p(\theta | \mathbf{X})$, and f is designed to be invertible and have a tractable Jacobian. By doing this, we can evaluate the posterior from $\pi(z)$ by change of variables. We choose a multivariate Gaussian for $\pi(z)$ as it makes the posterior easy to sample and evaluate. `Haloflow` uses masked autoregressive flows (MAFs; G. Papamakarios et al. 2018), a type of normalizing flow that model a complex distribution using a series of invertible autoregressive transformations.

We train a flow, q_ϕ , with hyperparameters, ϕ , to best approximate $q_\phi(\theta | \mathbf{X}) \approx p(\theta | \mathbf{X})$. For each galaxy $\{(\theta_i, \mathbf{X}_i)\}$ in the training set, we maximise the total log-likelihood $\sum_i \log q_\phi(\theta_i | \mathbf{X}_i)$. This is equivalent to minimizing the Kullback-Leibler divergence between $p(\theta | \mathbf{X})p(\mathbf{X})$ and $q_\phi(\theta | \mathbf{X})p(\mathbf{X})$. To determine the final normalising flow, `Haloflow` employs an ensemble of independently initialized and trained flows for the final NPE for improved accuracy (B. Lakshminarayanan et al. 2019; J. Alsing et al. 2019).

q_ϕ implicitly encodes a prior, $p(\theta)$, which is set by M_* and M_h distributions of the training data. Without correction, this implicit prior mirrors the underlying stellar and halo mass functions, biasing inferred posteriors toward low M_* and low M_h , where galaxies are more abundant. We correct this prior and impose uniform priors in $\log M_*$ and $\log M_h$ using the W. Handley & M. Millea (2019) maximum entropy prior method. In practice, for each posterior sample, $\theta' \sim p(\theta' | \mathbf{X})$, we apply an importance weight, $1/p(\theta')$ to ensure that we have uniform priors on M_* and M_h .

C. Hahn et al. (2024) estimated $p(\theta')$ using a binned halo mass function and linearly interpolating it to evaluate at each θ' . The halo mass function is sparsely populated at the high-mass end, leading to noisy estimates of $p(\theta')$ and consequently large, unstable importance weights, further exacerbated by increased flow uncertainty in the posterior tails. To stabilise the correction, we fit a single Schechter profile to the halo mass function and use this smooth analytical form to model $p(\theta')$. Additionally, before applying the prior reweighting, we discard posterior samples lying beyond the 0.5th and 99.5th percentiles of the NPE posterior. This removes poorly constrained extreme tail samples that would otherwise generate pathological weights. Together, these modifications yield numerically stable, prior-corrected posteriors (see Appendix A for details).

In this work, we adopt the `Haloflow` framework and maintain the same parameter space as in C. Hahn et al. (2024). We also use the same network architecture

¹⁰ also known as implicit likelihood inference

and hyperparameter optimization procedure as C. Hahn et al. (2024). We extend the original methodology to incorporate a broader range of galaxy features extracted from synthetic images across multiple simulations (see §2.1 and Table 1).

3.2. Domain Adaptation

SBI methods rely on the assumption that the training and test data are drawn from the same distribution. However, this assumption is often violated in practice, particularly when flows trained on synthetic data are applied to real observations. Even across different simulations, variations in galaxy-formation physics, numerical resolution, numerical scheme and calibration can lead to systematic differences in the observable properties of galaxies. If unaddressed, these discrepancies lead to model misspecification.

Since the true generative process of the Universe is unknown, some level of model misspecification is unavoidable. To mitigate its effects, we introduce DA as an intermediate step before performing SBI. The goal of DA is to map galaxy features \mathbf{X} into a representation space where their distributions are statistically aligned across different domains, $c\mathbf{X}$ – in our case, across different simulations. By learning domain-invariant features, the posterior estimator becomes less sensitive to simulation-specific artifacts, improving robustness and generalisation.

In this work, we study two unsupervised DA techniques: (1) Domain Adversarial Neural Networks (DANN, §3.2.1 Y. Ganin et al. 2017), which use adversarial learning to promote domain invariance, and Maximum Mean Discrepancy (MMD, §3.2.2 A. Gretton et al. 2008), which directly minimizes distributional differences between domains using kernel-based distance metrics. In Figure 2, we show a schematic overview of our DA setup. Together, these components define the DA extension of `Haloflow`^{DA}. The original `Haloflow` pipeline is applied not to the raw features \mathbf{X} but to compressed, DA-informed representations $c\mathbf{X}$ produced by the DANN or MMD networks.

3.2.1. Domain Adversarial Neural Networks

DANNs are a technique for unsupervised DA that aims to address model misspecification through adversarial training. The goal is to learn a feature representation that is *invariant* across different simulations, while still retaining the information needed to predict physical parameters, θ . DANN introduces an adversarial training setup composed of three parts: a “feature extractor” that maps \mathbf{X} into a lower-dimensional latent representation $c\mathbf{X}$; a “regressor” that uses the latent representation to estimate θ ; and a “domain classifier” that tries

to determine which simulation $c\mathbf{X}$ came from. Crucially, the feature extractor is optimised adversarially: it is updated so as to make the domain classifier’s task harder. This forces the extractor to learn domain-invariant features that contain physical information relevant for inference but suppress simulation-specific information.

To implement this adversarial setup, we use a gradient reversal layer (GRL). This layer behaves as the identity function during the forward pass, but multiplies the gradient by a negative scalar during backpropagation. As a result, the feature extractor is updated in a direction that maximally confuses the domain classifier, i.e., it attempts to remove the domain-specific information in the learned features.

The overall loss function is:

$$\mathcal{L} = \mathcal{L}_{\text{reg}} + \lambda \mathcal{L}_{\text{DA}} \quad (1)$$

where \mathcal{L}_{reg} is the regression loss; \mathcal{L}_{DA} is the domain classification loss; and λ controls the relative strength of the domain-adversarial signal during training.

We define the regression loss as a weighted mean squared error (MSE):

$$\mathcal{L}_{\text{reg}} = \sum_{i=1}^N w_i \|\hat{\theta}_i - \theta_i\|^2 \quad (2)$$

where $\hat{\theta}_i$ is the predicted parameter vector, θ_i is the ground truth from the simulation. The weighting is introduced to prevent the model from being dominated by regions of parameter space that are overrepresented in the training data, particularly low-mass halos and to ensure adequate performance across domains across the full mass range. Without the weighting, the network would preferentially optimise accuracy where data are most abundant, i.e., at the expense of high-mass. The per-sample weight, w_i , therefore up-weights underrepresented domains and halo-mass ranges while down-weighting overrepresented ones; w_i is the product of a domain-balancing term and a mass-dependent term based on an inverse Schechter-like function of halo mass (see Appendix B for details).

The domain classification loss is a categorical cross-entropy:

$$\mathcal{L}_{\text{DA}} = - \sum_{i=1}^N \sum_{j=1}^K y_{ij} \log(p_{ij}) \quad (3)$$

where K is the number of simulations, y_{ij} is a one-hot encoded vector indicating the true simulation source, p_{ij} is the predicted probability that sample i came from simulation j . This loss is minimised by the domain classifier but maximised by the feature extractor via GRL. This adversarial objective ensures that the learned features do not encode which simulation a galaxy came from.

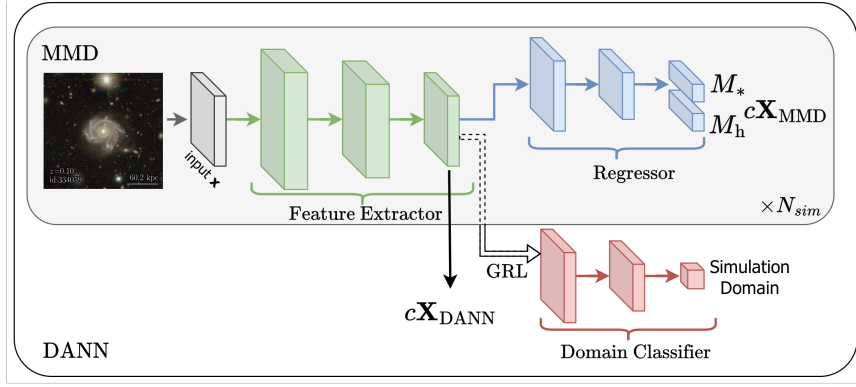


Figure 2. Schematic of the DA frameworks used in this work. Images of galaxies are preprocessed into input features, \mathbf{X} , which are passed through a feature extractor (green), and a regressor (blue) to predict M_* and M_h for each simulated galaxy. The dark gray panel (MMD) applies a MMD loss in the latent feature space, while the white panel (DANN) routes the extracted features through a gradient reversal layer to a domain-classifier network (red) that predicts which simulation the galaxy from and encourages domain-invariant features. The compressed domain features, $c\mathbf{X}$, used in `HaloflowDA` are taken from the feature-extractor (32-dimensional) for the DANN runs, and from the label-predictor output (2-dimensional, (M_*, M_h)) for the MMD runs.

To stabilize training, we gradually increase the strength of the adversarial signal during training. Specifically, we set:

$$\lambda(p) = \frac{2}{1 + \exp(-4.5 \cdot p)} - 1, \quad \text{where } p = \frac{\text{epoch}}{\text{total}} \quad (4)$$

This function smoothly increases λ from 0 to 1 over the course of training, allowing DANN to first focus on learning the regression task before being strongly penalized for domain information. This schedule was found empirically to stabilize training and improve final inference performance (see §5 for further details).

For the compressed representation of observed features $c\mathbf{X}$ used as input for our SBI, we use the 32-dimensional z output of the DANN feature extractor.

3.2.2. Maximum Mean Discrepancy (MMD)

MMD is a kernel-based method for unsupervised DA. It provides a non-adversarial approach to learning domain-invariant features by directly minimizing a statistical distance between feature distributions from different simulations.

In our setup, MMD is used to reduce differences in the *latent* features extracted by the network across simulations with different galaxy formation models. An MLP feature extractor maps the observational feature vector \mathbf{X} to a 32-dimensional representation \mathbf{z} (see Appendix C). A separate regressor then maps \mathbf{z} to the two outputs (M_*, M_h) . By minimizing this discrepancy between the \mathbf{z} distributions of different simulations, the model is encouraged to focus on physical properties shared across simulations, rather than features tied to simulation-specific details, which can improve generalization to out-of-domain data.

The core idea behind MMD is to embed the \mathbf{z} distributions from different simulations into a reproducing kernel Hilbert space (RKHS), where comparisons between distributions can be made using kernel functions. In this space, MMD measures the squared distance between the mean embeddings of two distributions; if the MMD is small (close to zero), the corresponding feature distributions are considered statistically aligned.

We adopt a Gaussian Radial Basis Function (RBF) kernel to measure similarity between pairs of latent features,

$$k(\mathbf{z}, \mathbf{z}') = \exp\left(-\frac{\|\mathbf{z} - \mathbf{z}'\|^2}{2\sigma^2}\right), \quad (5)$$

and fix the kernel bandwidth to $\sigma = 1.0$ and the MMD weight to $\lambda = 0.5$ for all experiments. These values were chosen based on a small grid search over (λ, σ) , which showed that the validation losses are relatively insensitive to modest variations in either parameter (Appendix C.3).

During training, we consider three simulations simultaneously: two source domain, A and B , and one target domain, C . We compute latent features, \mathbf{z}_A , \mathbf{z}_B , \mathbf{z}_C by passing \mathbf{X}_A , \mathbf{X}_B , and \mathbf{X}_C through a shared feature extractor. The DA loss is then defined as the sum of the squared MMD distances between the target and each source,

$$\mathcal{L}_{\text{DA}} = \text{MMD}^2(\mathbf{z}_A, \mathbf{z}_C) + \text{MMD}^2(\mathbf{z}_B, \mathbf{z}_C), \quad (6)$$

where each MMD^2 term is computed using the RBF kernel above. This loss encourages the latent features of both training simulations to align with those of the target simulation. The three-way setup reduces the risk that the network overfits to a single simulation and provides a simple proxy for the situation in which real ob-

servations occupy an intermediate regime between simulations.

The final training objective for the MMD model has the same form as Eq. 1:

$$\mathcal{L} = \mathcal{L}_{\text{reg}} + \lambda \mathcal{L}_{\text{DA}}. \quad (7)$$

The regression loss \mathcal{L}_{reg} is defined as in Eq. 2, using only the two training simulations (A and B) and the same per-sample weights w_i described in Appendix B. We emphasize that the test simulation C enters only through the MMD term; hence, we do not use any M_* or M_h information of the test simulation. We fix $\lambda = 0.5$, which we find provides a good balance between fitting the regression task and enforcing cross-domain alignment.

For $c\mathbf{X}$ used as input to our SBI, we use the 2D regressor output. Implementation details of the MMD architecture and training hyperparameters are described in Appendix C.

3.2.3. *HaloFlow*^{DA}: Domain-Adapted Posterior Inference

For test simulation C , we designate the two other simulations, A and B , as training domains. A DA model (DANN or MMD) is then trained using labeled samples from A and B and unlabeled samples from C . Once trained, the DA network is frozen and used purely as a feature extractor. We apply the frozen DA network to galaxies from simulations A and B to obtain compressed, domain-adapted representations $c\mathbf{X}_A$ and $c\mathbf{X}_B$, and we likewise compute $c\mathbf{X}_C$ for the target simulation. For the DANN runs, $c\mathbf{X}$ is taken to be the 32-dimensional latent output of the feature extractor; for the MMD runs, $c\mathbf{X}$ is taken to be the 2-dimensional regressor output.

We then train *HaloFlow* in two separate NPEs: one using training pairs $(c\mathbf{X}_A, \theta_A)$, and the other using $(c\mathbf{X}_B, \theta_B)$. The key difference relative to the standard setup is that, instead of conditioning on the raw features \mathbf{X} listed in Table 1, *HaloFlow*^{DA} learns posteriors conditioned on the compressed representations $c\mathbf{X}$. Finally, we evaluate each trained NPE on the held-out test simulation C . C is never used for training the NPE. It enters only through the DA stage as an unlabeled target domain.

This setup provides a controlled testbed for assessing whether DA can improve generalization to out-of-domain data. In particular, we can examine how DA impacts the calibration, accuracy, and uncertainty of the resulting posteriors across different choices of train-test simulation combinations ($A, B \rightarrow C$).

To illustrate the effect of DA, we use Uniform Manifold Approximation and Projection (UMAP; L. McInnes et al. 2020) to project the high-dimensional feature space

into two dimensions. Figure 3 shows the feature distributions before (left) and after (right) DA. Without DA, features from different simulations occupy distinct regions in the projected space, indicating a domain shift between them. After applying DA, the features are significantly more aligned, with much greater overlap between the simulations. This alignment suggests that the DA model successfully learns a representation that is less sensitive to simulation-specific effects.

4. RESULTS

We now assess the performance of *HaloFlow* and its domain-adaptive extension, *HaloFlow*^{DA}, in inferring halo masses across different simulation domains.

4.1. Domain Shift Degrades Posterior Inference

Figure 4 illustrates the impact of domain shift on M_h posteriors. Here, *HaloFlow* is trained on TNG, and tested on both TNG (in-domain; blue) and EAGLE (out-of-domain; red). In the in-domain case, inferred M_h closely match the true values, with 77% of the halos lie within their quoted 1σ interval of the posterior, consistent with slightly conservative but well-calibrated posteriors. However, when *HaloFlow* is applied to the out-of-domain, the M_h posteriors become substantially less reliable with only 48% within their quoted 1σ interval of the posterior. The posteriors are significantly overconfident under the domain shift.

As additional validation, we perform a “data to random point” (DRP; P. Lemos et al. 2023) coverage test. For each sample, we evaluate distances between the samples drawn from the two NPEs with a random point in parameter space. We compare this distance to the distance between the true parameter values and the random point to derive an estimate of the expected coverage probability. In the right panel of Figure 4, we present a quantitative assessment of the posteriors using DRP coverage plots. In the in-domain case, the predicted posteriors yield near-ideal coverage (close to the black dashed one-to-one line), implying that *HaloFlow* provides near optimal estimates of the true posteriors. However, in the out-of-domain case, coverage falls below the ideal diagonal, confirming that the posteriors from the NPE is overconfident and underestimates the uncertainties.

To more directly quantify inference performance in the context of DA, we define a normalised residual,

$$\beta = \frac{|m - \hat{m}|}{\sigma_{\hat{m}}} \quad (8)$$

where \hat{m} and $\sigma_{\hat{m}}$ are the median and standard deviation of the NPE M_h posteriors and m is the true M_h . For

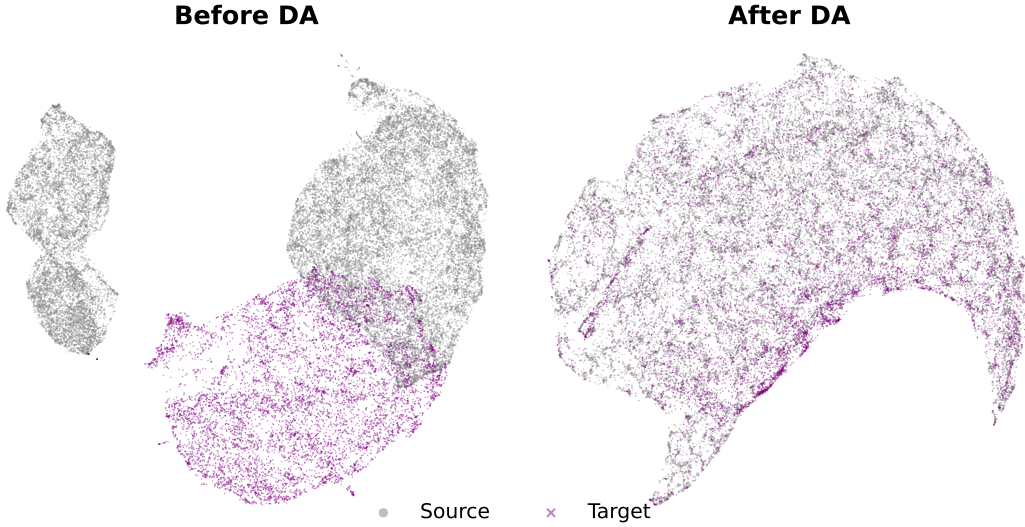


Figure 3. UMAP showing the distribution of source (gray) and target (purple) simulations before DA (left) and after DA (right). Before DA the source and target distributions are highly discrepant. After DA the source and target distributions are indistinguishable suggesting that they are domain-invariant to each other.

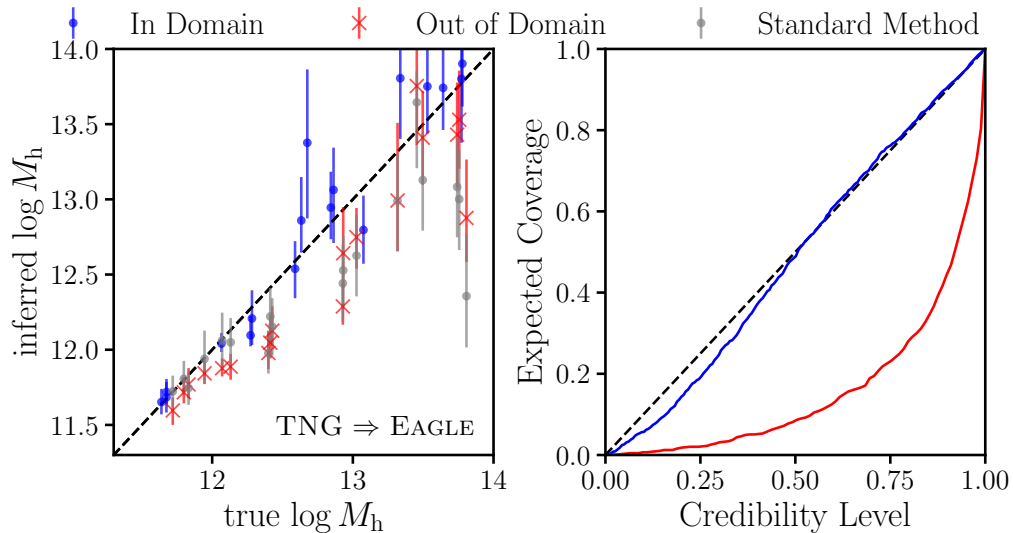


Figure 4. Left: Inferred vs. true M_h using `HaloFlow` trained in-domain (blue; TNG \Rightarrow TNG) and out-of domain (red; TNG \Rightarrow EAGLE). Predictions are accurate and well-calibrated in the in-domain case, but show systematic bias under domain shift. For reference, we include M_h constraints using the standard approach based on the SHMR applied out-of-domain (gray). The standard approach also exhibits significant systematic bias. **Right:** Coverage plots for the `HaloFlow` posteriors. In-domain scenario shows near-ideal calibration (black dashed), while out-of-domain shows poorer calibration, indicating overconfident and unreliable posteriors.

an unbiased and perfectly calibrated Gaussian posterior, the median $\beta \simeq 0.67$. $\beta \ll 0.67$ indicate conservative uncertainties, while $\beta \gg 0.67$ signals overconfident or systematically biased posteriors. For the example in Figure 4, we find a median $\beta = 0.58$ for the in-domain case. In contrast, the out-of-domain scenario yields a median $\beta = 1.66$.

4.2. Domain Adaptation Improves Generalization

To test whether DA can improve inference across simulations, we apply both DANN and MMD-based adaptation to all train/test simulation combinations. We present our results in Figure 5. Each panel corresponds to a specific training (row) \Rightarrow testing (column) simulation. For each setup, we compare posterior medians (with 1σ error bars) for three NPEs:

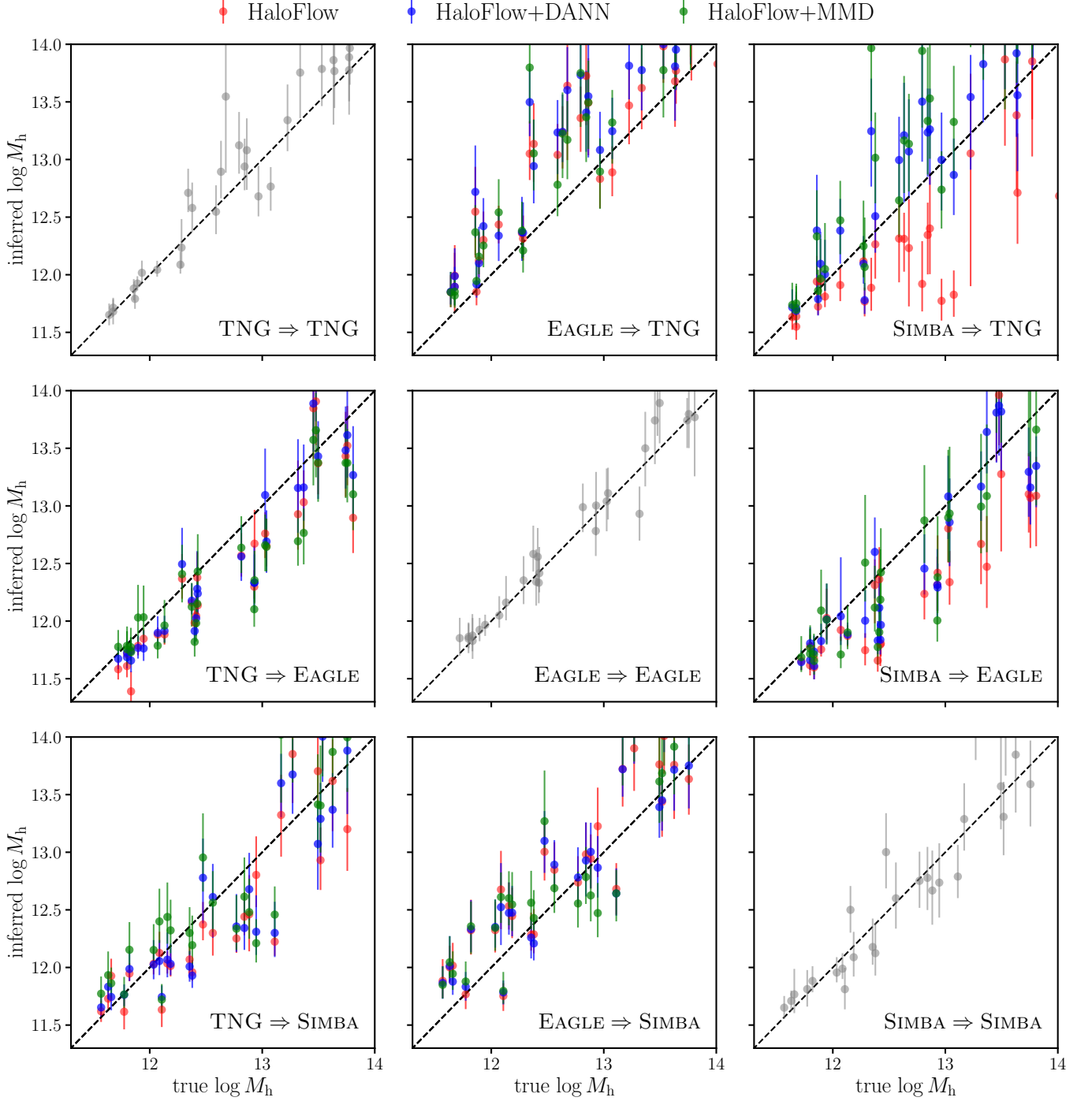


Figure 5. Inferred vs. true halo masses across all train \Rightarrow test simulation pairs. Each panel corresponds to one combination (row: test sim, column: train sim). Scatter points show median inferred M_h with 1σ errorbars from: **HaloFlow** only (red), **HaloFlow+DANN** (blue), and **HaloFlow+MMD** (green). Diagonal panels show in-domain inferences with **HaloFlow** (gray) for reference. Off-diagonal panels reveal model misspecification for **HaloFlow** (red) and demonstrate that DANN and MMD (blue and green) improve the robustness of M_h inference across simulations.

baseline `Haloflow` (red), `Haloflow+DANN` (blue) and `Haloflow+MMD` (green). We only plot a subset of galaxies in the simulations for clarity. For reference, we include in the diagonal panels the performance of `Haloflow` in-domain (gray).

In off-diagonal cases (out-of-domain), where the test simulation differs from the training simulations, we find systematic deviations for `Haloflow` alone—especially in `SIMBA \Rightarrow TNG` and `SIMBA \Rightarrow EAGLE`, where the median β increases to 1.11 and 1.62, respectively. Both DA methods significantly reduce these biases and improve calibration where β is 0.64 and 0.70 respectively. Moreover, both exhibit adaptive uncertainty behavior: in many cross-domain cases the posterior error bars are widened relative to the in-domain baseline, particularly where the bias and scatter are largest, and remain narrower when the predictions are closer to the one-to-one line. Overall, DA significantly improves the generalization of `Haloflow`, yielding more robust and better calibrated posteriors across simulations.

To quantitatively assess the effect of DA, we compute the median β of M_h for all train \Rightarrow test pairs, shown in Table 2. For a baseline reference, in-domain scenarios (diagonal entries), posteriors from the baseline `Haloflow` have $\beta \approx 0.5$ – 0.6 . In out-of-domain settings, both DANN and MMD reduce β in nearly all cases, indicating improved inference quality. We also show the fraction of halos whose masses are within 1σ of the estimated posteriors for each of the runs in Table 3.

MMD consistently outperforms DANN, achieving the lowest β across all simulation combinations. The most dramatic improvement occurs for the `SIMBA \Rightarrow EAGLE` transfer, where β drops from 1.62 (no DA) to 0.70 (with MMD) – a 57% reduction. This highlights the effectiveness of MMD in aligning feature distributions across physically different simulations. DANN also yields meaningful improvements, particularly when training on TNG or SIMBA. However, its performance is less consistent: for instance, when trained on EAGLE, DANN slightly increases β , suggesting some instability in the adversarial training process.

To benchmark DA further, we compare it against the standard approach based on the stellar–halo mass relation (SHMR). To mimic the standard approach, we use `Haloflow` trained on the training simulation to obtain a posterior over stellar mass from photometry in the test simulation. This step is analogous to conventional SED modeling. Then we draw samples $M'_* \sim p(M_* | X_{\text{mags}})$ and propagate them through the training simulation’s SMHR to infer halo masses. In Figure 6, we compare the precision (left) and β (right) of the M_h posteriors derived from `Haloflow`^{DA} (green, MMD; blue, DANN)

versus the standard method (gray dashed) as a function of M_* . The posteriors are for the `TNG \Rightarrow EAGLE` scenario. We use the standard deviation of the M_h posterior ($\sigma_{\log M_h}$) to represent precision of the posterior. `Haloflow`^{DA} achieves precision comparable to the standard method. The `Haloflow`^{DA} run with MMD also shows improvement in β (0.76 compared to 0.94 for the standard method). The horizontal dashed lines represent the overall median β for all three runs and the black solid represents an unbiased and perfectly calibrated posterior ($\beta \simeq 0.67$). Overall, `Haloflow`^{DA} provides a more robust and less biased inference than the standard method, without sacrificing precision.

5. DISCUSSION

We investigate how domain shifts among different simulations impact M_h inference when using `Haloflow`. Having established that DA improves the robustness of M_h posteriors out-of-domain, we next examine (i) the role of the DA loss weight λ , (ii) where DA should be applied within the network, (iii) the resulting posterior calibration and uncertainties, (iv) implications for information-maximizing compression methods more broadly, and (v) fundamental limitations of DA across physically distinct models.

5.1. Sensitivity to the DA loss λ

The parameter λ in Eq. 1 plays a crucial role in balancing the trade-off between enforcing domain invariance and preserving information relevant for inferring M_h . To probe this trade-off, we varied λ for some of the worst-performing out-of-domain transfers (highest median β in Table 2).

When λ is large ($\gtrsim 1$), the DA network places more emphasis on aligning feature distributions across domains, effectively minimizing differences in the simulations. While this improves robustness to domain shift, it degrades feature extraction by discarding features that are informative for M_h , leading to broader posteriors. Conversely, when λ is small (< 1), the network prioritizes minimizing the regression loss, retaining more M_h -relevant information but becoming more sensitive to discrepancies between domains. In the limit $\lambda = 0$, the DA objective vanishes and the network performs a lossy compression of the input features \mathbf{X} without any domain adaptation; the method reduces to standard `Haloflow` with data compression.

In practice, we find that the behavior of λ depends strongly on the choice of DA method. For DANN, tuning λ proved challenging due to inherent instability of adversarial training. As λ increases, the domain classifier becomes increasingly dominant, often overpowering

Table 2. Median β of M_h for all train/test simulation pairs. Rows indicate test simulations, columns indicate train simulations, matching the layout of Figure 5. Values are reported as HaloFlow / HaloFlow+DANN / HaloFlow+MMD. Diagonal entries correspond to in-domain performance where DA is not applied. Bold values indicate best (lowest) β for each pair.

Test \ Train	TNG	Eagle	Simba
TNG	0.58 / — / —	1.26 / 1.38 / 1.10	1.11 / 0.89 / 0.64
Eagle	1.66 / 1.18 / 0.76	0.54 / — / —	1.62 / 1.06 / 0.70
Simba	1.12 / 0.95 / 0.94	1.37 / 1.50 / 1.32	0.58 / — / —

Table 3. Fraction of halos within the quoted 1σ interval of the posterior. Layout of this table matches Table 2. Bold values indicate the highest fraction for each pair.

Test \ Train	TNG	Eagle	Simba
TNG	0.75 / — / —	0.35 / 0.31 / 0.46	0.46 / 0.58 / 0.70
Eagle	0.31 / 0.44 / 0.60	0.80 / — / —	0.32 / 0.48 / 0.64
Simba	0.45 / 0.52 / 0.53	0.34 / 0.30 / 0.37	0.76 / — / —

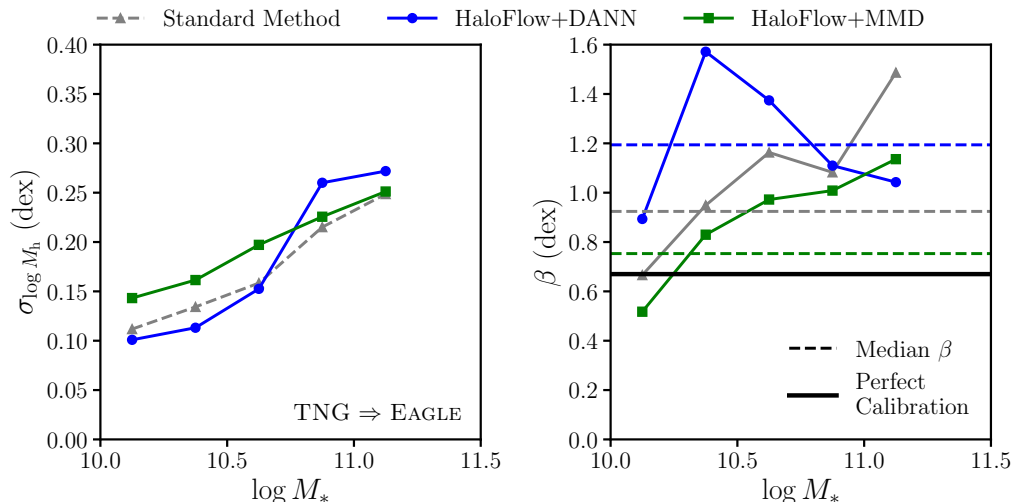


Figure 6. Comparison of the precision (left) and bias (right) of M_h posteriors inferred using HaloFlow^{DA} (MMD, green; DANN, blue) and the standard method based on the SHMR for the TNG \Rightarrow EAGLE scenario. **Left:** Median 1σ of the M_h posteriors ($\sigma_{\log M_h}$), as a function of M_* . Both the HaloFlow^{DA} methods yield similar precision to that of the standard method even during out-of-domain inference. **Right:** Median β as a function of M_* . The dashed lines represent the median β for the complete test set. The black bold line is the $\beta \simeq 0.67$ for a perfectly calibrated posterior. The posteriors from HaloFlow^{DA} using MMD is closer to optimally calibrated posteriors than that of the standard method while maintaining comparable precision.

the feature extraction. While we followed the scheduling for λ from Y. Ganin et al. (2017), ramping up λ gradually (see Eq. 4), we observed substantial variability in the performance based on the choice of training and test domains. In some cases, this led to higher median β values than the baseline HaloFlow when applied to out-of-domain simulations, particularly for runs in EAGLE \Rightarrow TNG or SIMBA.

In contrast, the MMD-based method was substantially more stable across a wide range of λ values. After testing several configurations, we found that a fixed $\lambda = 0.5$ consistently yielded reliable performance across all simula-

tion pairs. This suggests that the kernel-based approach of MMD, which avoids adversarial dynamics entirely, offers a more robust solution in data-limited regimes or when simulation differences are pronounced (more details in Appendix C.3).

5.2. Where to apply DA?

While DA can mitigate discrepancies between domains, we found that its success highly depends on *where* and *how* the compressed features for HaloFlow^{DA} are defined, consistent with previous work (H. Zhao et al. 2019; A. Sicilia et al. 2023). Early in our experiments,

we attempted to enforce domain invariance on a highly compressed representation, using the two-dimensional regressor output, $\hat{\theta}$. For DANN, this configuration performed poorly, producing larger bias β values than the baseline. A larger value of β does not necessarily imply a narrower posterior; instead it means that the absolute error increased relative to the inferred uncertainty. This likely occurred because enforcing strict domain invariance at such a low-dimensional stage discarded information essential for accurate inference: by forcing $\hat{\theta}$ to appear similar across simulations, the network lost flexibility to account for subtle but physically meaningful variations in galaxy properties.

Interestingly, the same approach using MMD performed substantially better. Even with this extreme compression, the distribution-level alignment on $\hat{\theta}$ preserved enough θ -informative structure to yield stable and relatively accurate posterior estimates. This contrast suggests that the alignment, which relies on a classifier-based criterion, is highly sensitive to the dimensionality of the features, whereas the distribution-matching approach is more robust to where alignment occurs within the processing pipeline.

Our final DA inference uses the compressed DA features differently depending on the method. For DANN, we perform DA at the level of the higher-dimensional embedding produced by the feature extractor, which encodes galaxy morphology, colors, and other parameters that remain informative for M_h estimation. This richer representation allows learning of domain-invariant yet physically meaningful features, improving stability and posterior accuracy. By contrast, the MMD approach achieves effective DA when applied to the regressor output, aligning simulations in the space of predicted quantities without substantial information loss.

5.3. Posterior calibration, uncertainty and robustness

A useful property of both DA methods is that neither increases posterior uncertainty arbitrarily. In fact, both approaches produce uncertainty estimates that are adaptively narrower when the inferred M_h is accurate and wider in ambiguous or poorly calibrated regions. This behavior is consistent with our training objective: the DA losses act only on the internal feature representations, while the posterior over M_h is still constrained for simulated pairs (\mathbf{X}, θ) . Where the target-domain data resemble the training simulations, DA primarily removes domain-dependent shifts without reducing the information content, so the posteriors remain tight but better calibrated. In regions where the simulations disagree more strongly or the mapping between galaxy properties and M_h is less well constrained, DA prevents

the network from extrapolating aggressively, leading to broader, more conservative posteriors.

5.4. Implications for information-maximizing compression

These insights extend beyond the specific methods discussed here. Neural networks are commonly used in astronomy and cosmology for compressing data into informative summaries for inference, such as Information Maximising Neural Networks (IMNNs; *e.g.*, T. Charnock et al. 2018; T. L. Makinen et al. 2021; T. Lucas Makinen et al. 2025), Moment Networks (N. Jeffrey & B. D. Wandelt 2020), or convolutional neural networks (CNNs) applied directly to maps and images (*e.g.*, C. Hahn et al. 2023; L. Eisert et al. 2024). These methods all face the same challenges as `Haloflow` when training and testing data differ due to domain shifts.

Without explicit DA, their summaries can fail to capture all of the parameter information present in the data once the domain shifts, leading to degraded inference. Moreover, compressing to very low-dimensional summaries can make this problem worse and can also make DA more susceptible. As discussed above, our experiments with DANN on a compressed representation yielded more biased inference than the baseline `Haloflow`. Kernel-based approaches such as MMD mitigated these issues and often improved robustness in our tests, but they do not *eliminate* simulation mismatch entirely. The broader takeaway is that studies using compressors should explicitly assess how domain shifts affect their compressed features and the resulting posteriors, and cannot assume that a summary that works well on the training simulations will remain reliable out-of-domain.

5.5. Limitations of DA

Although `Haloflow`^{DA} improves the overall robustness of the M_h inference, its performance still depends on the degree of physical mismatch between simulations. For instance, `SIMBA` implements more aggressive AGN feedback than either `TNG` or `EAGLE`; in `SIMBA`, this leads to earlier quenching and alters their stellar mass and gas content at fixed M_h (M. Ayromlou et al. 2023; R. J. Wright et al. 2024), making `SIMBA` a particularly challenging target. When training on `EAGLE` and testing on `SIMBA`, the baseline `Haloflow` yields a median $\beta = 1.37$, higher than for most other simulation pairs. DA does not significantly improve the robustness ($\beta_{\text{MMD}} = 1.32$), which suggests that DA cannot fully account for divergences in the underlying physical models.

Even if DA brings the feature distributions closer together, it cannot fully remove the mismatch because the underlying galaxy–halo connection itself is different. In

practice, DA can shift and reweight the existing distributions so that simulations look more alike, but it cannot generate physical behavior that is absent from the training simulations. This also implies that DA only works well if the training data used for DA encompasses that of the test set. In future work, when we apply `HaloflowDA` to observations, we are assuming that it lies somewhere in between of all the training simulations.

There are further caveats. Our results are based on only three hydrodynamical simulation suites: TNG, EAGLE, and SIMBA. While these represent a range of subgrid physics, they do not span the full space of plausible galaxy formation models. This limits our ability to fully assess how DA performs across more extreme physical priors. Expanding the training and testing set to include additional simulations—especially those with varied feedback implementations or alternative dark matter models—will be important for testing the generality of our approach.

This study focuses exclusively on central galaxies with stellar masses above $M_* > 10^{10} M_\odot$ at $z = 0.1$. This selection limits our conclusions. Lower-mass galaxies, satellites, or higher-redshift populations could exhibit stronger or weaker domain shifts. Our results should therefore be interpreted as demonstration on a specific galaxy population and direct future applications of it can only be applied to consistent galaxy populations. We, however, emphasize that the `HaloflowDA` can be easily extended by incorporating other galaxy populations in the training.

Despite these caveats, the improvements shown by `HaloflowDA` suggest that these techniques will be valuable when applying simulation-trained models to real galaxy observations. Domain shift is unavoidable in observational settings due to differences in measurement noise, selection effects, and the fact that no simulation perfectly captures the physics of galaxy formation. While our experiments are limited to a small set of hydro simulations, the consistent gains from MMD-based adaptation indicate that even approximate alignment of latent feature distributions can improve out-of-domain performance. This opens the possibility of applying `HaloflowDA` to real HSC-SSP observations.

6. CONCLUSIONS

In this work, we introduced `HaloflowDA`, a domain-adapted extension of the `Haloflow` framework that combines SBI with DA to improve the robustness of M_h inference from galaxy photometry and morphology. Using forward-modeled HSC-like galaxy images from three state-of-the-art hydrodynamical simulations, TNG, EAGLE, and SIMBA, we showed that the stan-

dard `Haloflow` M_h posteriors are robust when we train and test on the same simulations but become biased and overconfident when applied across simulations. This degradation arises from domain shift: each simulation encodes a different galaxy formation model and, thus, induces a different mapping between galaxy observables and M_h .

To address this, `HaloflowDA` learns domain-adapted representations of galaxy observables that retain the information relevant for M_h inference while suppressing features specific to individual simulations. We implemented two DA strategies: DANN and MMD. DANN and MMD both aim to align these representations. DANN does this adversarially by training a feature extractor to “fool” a domain classifier, while MMD minimizes a statistical distance between the train and test domains’ feature distributions directly. Once the DA network is trained, its domain-adapted representations $c\mathbf{X}$ are input into the `Haloflow` SBI framework to produce M_* and M_h posteriors.

To quantify the performance of `HaloflowDA`, we apply it across all train \Rightarrow test simulation pair combinations of TNG, EAGLE, and SIMBA. Our main findings are:

- **Domain shift significantly degrades M_h posteriors, but DA substantially improves robustness.** In-domain applications of `Haloflow` yield well-behaved M_h posteriors with median $\beta \simeq 0.5$ – 0.6 and near-ideal coverage. Out-of-domain, median $\beta \lesssim 1$ – 1.5 , indicating biased and overconfident posteriors. `HaloflowDA` systematically reduces these failures: both DANN and MMD lower β in nearly all test cases.
- **The architecture of the DA matters; kernel-based MMD is particularly robust.** The impact of DA depends on both the method and the representation on which alignment is enforced. DANN, which uses adversarial training, is sensitive to the strength of the DA loss and to the dimensionality of the aligned features. MMD, by contrast, is substantially more robust: a simple configuration with fixed $\lambda = 0.5$ and RBF kernel bandwidth $\sigma = 1.0$ consistently reduces β across all train \Rightarrow test combinations and achieves the best overall performance.
- **DA improves robustness but cannot fully compensate for physical mismatches.** The effectiveness of `HaloflowDA` is limited by differences in the underlying galaxy–halo connection. SIMBA, for example, has more aggressive AGN feedback than TNG and EAGLE, which makes it a more challenging test domain. In this case, DA improves

β , but not comparable to in-domain performance. DA can align observable feature distributions and reduce systematic biases, but it cannot generate physical behavior absent from the training simulations. Thus, the success of `HaloflowDA` ultimately depends on training over a set of simulations that plausibly bracket the real Universe.

These results demonstrate that DA is necessary in making simulation-based M_h inference robust to the inevitable mismatches between simulations and reality. Although our experiments are restricted to three hydrodynamical suites and to central galaxies with $M_* > 10^{10}, M_\odot$ at $z = 0.1$, they provide a concrete demonstra-

tion: even approximate alignment of latent feature distributions via MMD-based DA leads to more accurate, better-calibrated posteriors in out-of-domain settings.

In future work, we will test the `HaloflowDA` M_h constraints of observed galaxies and groups in HSC-SSP against independent mass constraints from galaxy-galaxy weak lensing measurements (*e.g.*, [D. Rana et al. 2022](#)). We will also compare them to dynamical mass estimates of groups identified in GAMA ([S. P. Driver et al. 2022](#)). Once validated, we will apply `HaloflowDA` to intervening halos observed by the FLIMFLAM spectroscopic survey ([K.-G. Lee et al. 2022](#)), which targets FRB foreground fields, in order to improve constraints on the CGM baryonic fraction in those systems.

APPENDIX

A. CORRECTION OF HALO MASS PRIOR

The trained `HaloflowDA` NPE, $q_\phi(\theta | \mathbf{X})$, inherits an implicit prior over parameters, $p_{\text{imp}}(\theta)$, set by the distribution of the training set ([C. Hahn et al. 2024](#)). Because the training galaxies are distributed according to the underlying stellar- and halo-mass functions, $p_{\text{imp}}(\theta)$ reflects these functions. In this work, we seek to adopt a prior uniform in $\log M_*$ and $\log M_h$.

Following the maximum-entropy prior framework of [W. Handley & M. Millea \(2019\)](#), we reweight posterior samples to enforce a user-defined target prior $r(\theta)$. For posterior samples $\theta' \sim q_\phi(\theta | \mathbf{X})$, we assign importance weights

$$w(\theta') = \frac{r(\theta')}{p_{\text{imp}}(\theta')}, \quad (\text{A1})$$

which reduces to

$$w(\theta') \propto \frac{1}{p_{\text{imp}}(\theta')} \quad (\text{A2})$$

for a uniform target prior.

In practice, this correction is implemented via importance sampling and can become unstable when $p_{\text{imp}}(\theta)$ is poorly sampled, particularly in the high-mass regime of the training distribution where the stellar- and halo-mass functions are sparsely populated. This instability is driven by two effects: (i) numerical noise in the estimate of p_{imp} in the high-mass tail, where the halo mass function is sparsely sampled, and (ii) increased uncertainty of the NPE in the tails of the posterior. Because the correction scales as $1/p_{\text{imp}}$, both effects can produce a small number of samples with disproportionately large weights, causing the reweighted posterior to be dominated by rare tail draws.

We stabilise the implicit-prior correction in two ways. First, to reduce stochasticity in the high-mass tail of the halo-mass distribution, we replace the empirical estimate of the implicit prior with a smooth analytical approximation by fitting a single Schechter function to the training-set halo-mass distribution and evaluating p_{imp} from this fit. Second, to limit sensitivity to inaccuracies at the tails of the NPE, we truncate the posterior samples before applying the importance weights by discarding draws outside the central 99% interval in M_h (*i.e.* below the 0.5th percentile or above the 99.5th percentile of the sampled marginal distributions). Together, these steps substantially improve the numerical stability of the importance sampled posteriors. Below, we describe these two steps in further detail.

A.1. Fitting the intrinsic halo mass function

To reduce weight instabilities caused by noise in the empirical estimate of p_{imp} in the high-mass tail, we model the training-set halo-mass distribution with a single-Schechter function. In linear halo mass, the model is

$$\phi(M_h) = \phi_M \left(\frac{M_h}{M_h^{\text{char}}} \right)^\alpha \exp \left(-\frac{M_h}{M_h^{\text{char}}} \right), \quad (\text{A3})$$

where ϕ_M is the normalization, M_h^{char} is the characteristic halo mass, and α is the low-mass slope. Since inference is performed in logarithmic halo mass,

$$g \equiv \log_{10} M_h, \quad (\text{A4})$$

we work with the corresponding form per unit $\log_{10} M_h$,

$$\phi(g) = \ln(10) \phi_M 10^{(g - \log_{10} M_h^{\text{char}})(\alpha+1)} \exp \left[-10^{(g - \log_{10} M_h^{\text{char}})} \right]. \quad (\text{A5})$$

We bin the training-set halo masses in g with bin edges $\{g_i\}$ and observed counts y_i . We fit the Schechter parameters $\boldsymbol{\psi} = (\phi_M, \log_{10} M_h^{\text{char}}, \alpha)$ by maximizing the Poisson likelihood of the binned counts. The expected number of halos in bin i is

$$\mu_i(\boldsymbol{\psi}) = \int_{g_i}^{g_{i+1}} \phi(g | \boldsymbol{\psi}) dg, \quad (\text{A6})$$

and, dropping terms constant in $\boldsymbol{\psi}$, the negative log-likelihood minimized during fitting is

$$\mathcal{N}(\boldsymbol{\psi}) = \sum_i [\mu_i(\boldsymbol{\psi}) - y_i \ln \mu_i(\boldsymbol{\psi})]. \quad (\text{A7})$$

A.2. Regularized halo-mass importance weights

For a uniform target prior, the maximum-entropy prior correction implies importance weights $w(\theta') \propto 1/p_{\text{imp}}(\theta')$. We approximate the implicit prior over g using the fitted Schechter model evaluated at ten equally spaced bins within the range of the halo-mass function.

The maximum-likelihood parameters $\boldsymbol{\psi}_{\text{MLE}}$ define a smooth parametric estimate of the training-set halo-mass distribution. The corresponding expected counts per bin,

$$\mu_i^{\text{prior}} \equiv \mu_i(\boldsymbol{\psi}_{\text{MLE}}), \quad (\text{A8})$$

define a discrete binned prior mass

$$p_i^{\text{prior}} \equiv \frac{\mu_i^{\text{prior}}}{\sum_k \mu_k^{\text{prior}}}. \quad (\text{A9})$$

For a posterior sample $\theta^{(j)}$ with halo mass $g^{(j)}$, we identify the corresponding mass bin $i(j)$ and assign an importance weight

$$w_h^{(j)} \propto \frac{1}{p_{i(j)}^{\text{prior}}}. \quad (\text{A10})$$

To ensure numerical stability, halo masses are clipped to the fitted mass range prior to bin assignment, and a small positive floor is imposed on p_i^{prior} . Finally, for convenience, the weights are renormalized such that

$$\sum_j w_h^{(j)} = N_{\text{samp}}, \quad (\text{A11})$$

which preserves relative weighting and does not affect posterior expectations.

A.3. Truncation of NPE posterior tails

In addition to the scarcity of high-mass halos in the training data, a second source of numerical instability arises from increased uncertainty in the tails of the normalizing flow posteriors. While the NPEs provide accurate posterior estimates in regions well supported by the training data, the extreme tails of the posterior distributions are often less well-constrained. When combined with importance weighting, these poorly constrained regions can lead to inflated variances and unstable posterior summaries.

To mitigate this effect, we truncate the NPE posterior samples by removing the most uncertain tail regions *before* the importance weighting. Specifically, for each inferred posterior we compute the 0.5th and 99.5th percentiles of the marginal halo-mass posterior samples, denoted $M_h^{0.5}$ and $M_h^{99.5}$, and discard draws with $M_h < M_h^{0.5}$ or $M_h > M_h^{99.5}$. This truncation removes the region where we suspect the NPEs are least reliable, while preserving the central 99% of the posterior mass relevant for inference.

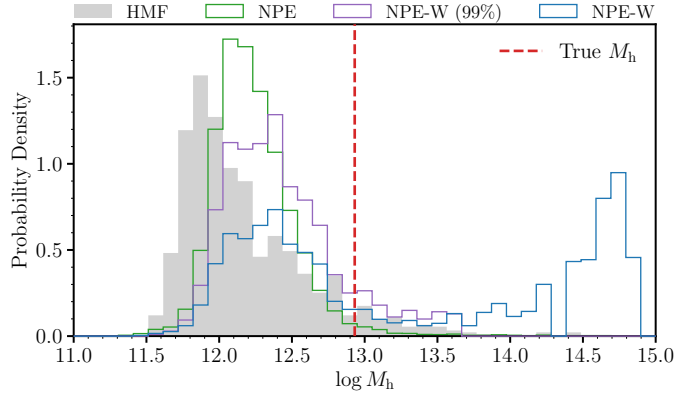


Figure 7. Comparison of halo-mass posterior distributions inferred using different methods. The gray histogram shows the intrinsic halo mass function (HMF) of the training data. The green curve corresponds to the unweighted NPE posterior. The blue curve shows the importance-weighted NPE posterior without truncation, which exhibits an amplified and unstable high-mass tail. The purple curve shows the importance-weighted NPE posterior after truncation at the central 99th percentile, yielding a stable distribution. The vertical red dashed line marks the true halo mass, M_h .

We emphasize that this truncation is applied before the importance weighting and does not introduce an explicit mass-dependent prior. Instead, it serves as a regularization step that limits the influence of regions where the posterior is poorly constrained.

Figure 7 illustrates the effect of importance weighting and posterior truncation on the inferred halo-mass distributions. The gray filled histogram shows the probability density of the intrinsic halo mass function of the training data. The green histogram corresponds to the unweighted `HaLoFlow`^{DA} NPE. The blue histogram corresponds to the importance-weighted NPE without any truncation. This histogram is amplified and unstable in the high-mass end. The purple curve shows the importance-weighted NPE with truncation at central 99th percentile where the distribution is much more stable in the high-mass tail. The red vertical dashed line represents the true M_h .

B. CONSTRUCTION OF DA SAMPLE WEIGHTS

In Eq. 2 we introduced per-sample weights w_i in the regression loss,

$$\mathcal{L}_{\text{reg}} = \sum_{i=1}^N w_i \|\hat{\theta}_i - \theta_i\|^2 \quad (\text{B12})$$

in order to (i) balance the relative contribution of different simulations (domains) and (ii) mitigate the strong imbalance in halo-mass sampling. Each weight is defined as the product of a domain-balancing factor and a mass-dependent factor,

$$w_i = w_{\text{dom}}(d_i) w_{\text{mass}}(M_{*,i}), \quad (\text{B13})$$

where d_i denotes the simulation (domain) of sample i and $M_{*,i}$ is its stellar mass.

B.1. Domain Balancing

Let $d \in 1, \dots, K$ index the simulations and N_d be the number of training samples from domain d . Without correction, domains with more samples would dominate the regression loss. To ensure that each domain has approximately equal influence on the loss, we assign each galaxy from domain d a domain weight

$$w_{\text{dom}}(d) \propto \frac{1}{N_d}. \quad (\text{B14})$$

In practice, this is implemented by constructing an array of domain sizes and computing

$$w_{\text{dom}}(d_i) = \frac{S}{N_{d_i}}, \quad (\text{B15})$$

where S is the sum of the distinct domain sizes. No additional global normalization is applied; the overall scale of w_{dom} is absorbed into the effective learning rate.

B.2. Mass-Dependent Weighting

Even within a given domain, the training-set is strongly imbalanced because it inherits the underlying halo-mass function, with low-mass halos greatly outnumbering high-mass halos. Without additional weighting, the loss in Eq. 2 would be dominated at the low-mass regime. To mitigate this imbalance, we construct a smooth parametric approximation to training-set mass distribution and up-weight underrepresented masses.

We model the one-dimensional training-set distribution in log-mass using the Schechter form in log space, $\phi(m)$, defined in Appendix A (Eq. A5). We fit the Schechter parameters to the combined training set by (i) forming a histogram of m using 20 uniform bins spanning the training-set range, (ii) converting bin counts to a density per dex (including the simulation volume normalization), and (iii) performing a non-linear least-squares fit to the binned density evaluated at the bin centers.

Given the fitted $\phi(m)$, we compute an unnormalized per-sample mass weight as the inverse of the fitted density evaluated at each sample,

$$\tilde{w}_{\text{mass}}(M, i) = \frac{1}{\phi(M, i)}. \quad (\text{B16})$$

We then rescale it by the minimum value across the training set so that the smallest mass weight is unity:

$$w_{\text{mass}}(M, i) = \frac{\tilde{w}_{\text{mass}}(M, i)}{\min_j \tilde{w}_{\text{mass}}(M, j)}. \quad (\text{B17})$$

and clip the mass-dependent weights from above to avoid excessively large values,

$$w_{\text{mass}}(M, i) = \min(w_{\text{mass}}(M, i), 10^2), \quad (\text{B18})$$

so that $w_{\text{mass}} \in [1, 10^2]$. No further normalization of w_{mass} is applied. The final per-sample weights used in Eq. 2 are then given by

$$w_i = w_{\text{dom}}(d_i), w_{\text{mass}}(M_{*, i}), \quad (\text{B19})$$

which up-weights underrepresented domains and the high-mass tail while down-weighting the most heavily populated regions of parameter space.

C. NETWORK ARCHITECTURES AND TRAINING HYPERPARAMETERS

C.1. DANN Architecture

The DANN model consists of three fully connected modules: a feature extractor that maps the input feature vector \mathbf{X} to a 32-dimensional latent representation, a label-predictor (regressor) that outputs (M_*, M_h) , and a domain classifier that predicts the simulation label. All hidden layers use SiLU activations. In the `HALOFLOWDA` pipeline, the 32-dimensional latent output of the feature extractor is used as the compressed representation $c\mathbf{X}$.

Table 4. DANN architecture. All hidden layers use SiLU activations.

Block	Layer	Output dim.	Activation
Feature extractor	Linear($d_{\text{in}}, 128$)	128	SiLU
	Linear(128, 64)	64	SiLU
	Linear(64, 32)	32	SiLU
Label predictor	Linear(32, 16)	16	SiLU
	Linear(16, 8)	8	SiLU
	Linear(8, 2)	2	—
Domain classifier	Linear(32, 16)	16	SiLU
	Linear(16, 8)	8	SiLU
	Linear(8, 4)	4	—

NOTE—The two outputs of the label predictor correspond to (M_*, M_h) . The four outputs of the domain classifier correspond to the simulations. The 32-dimensional latent features from the feature extractor are used as $c\mathbf{X}$.

C.2. MMD Architecture

The MMD model shares the same high-level structure as DANN but omits the domain classifier. It contains a feature extractor that maps \mathbf{X} to a 32-dimensional latent representation and a regressor that outputs (M_*, M_h) . The MMD loss is computed on the 32-dimensional latent features, while the 2-dimensional regressor output is used as $c\mathbf{X}$ in `HaloFlowDA`.

Table 5. MMD architecture. All hidden layers use SiLU activations.

Block	Layer	Output dim.	Activation
Feature extractor	Linear($d_{\text{in}}, 256$)	256	SiLU
	Linear(256, 128)	128	SiLU
	Linear(128, 64)	64	SiLU
	Linear(64, 32)	32	—
Label predictor	Linear(32, 16)	16	SiLU
	Linear(16, 8)	8	SiLU
	Linear(8, 2)	2	—

NOTE—The two outputs of the label predictor correspond to (M_*, M_h) . The 32-dimensional latent features from the feature extractor are used to compute the MMD loss (Eq. 6), while the 2-dimensional output of the label predictor is used as the compressed representation $c\mathbf{X}$ for the MMD runs.

C.3. Training Hyperparameters

Table 6 summarizes the main training hyperparameters used for the DANN and MMD runs. Unless otherwise noted, all other optimizer settings are left at their PyTorch defaults.

Table 6. Training hyperparameters for the DANN and MMD models.

Parameter	DANN	MMD
Optimizer	AdamW (I. Loshchilov & F. Hutter 2019)	AdamW
Learning rate	10^{-2}	10^{-4}
Weight decay	10^{-5}	5×10^{-4}
Max epochs	1000	350
Batching	full-batch (entire training set)	mini-batch, size 512
LR scheduler	ReduceLRonPlateau on val. loss (factor 0.5, patience 45)	none
Gradient clipping	global norm ≤ 1.0	none
Early stopping patience	50 epochs	10 epochs
DA weight λ	schedule $\lambda(p)$ (Eq. 4)	fixed $\lambda = 0.5$
Kernel bandwidth σ	—	fixed $\sigma = 1.0$

For DANN, we perform full-batch gradient updates: at each epoch the loss is evaluated over the entire training set before performing a single optimizer step. The learning rate is adapted using a `ReduceLRonPlateau` scheduler that monitors the validation loss and multiplies the learning rate by 0.5 whenever the validation loss fails to improve for 45 consecutive epochs. Early stopping with a patience of 50 epochs selects the final model.

For MMD, we use standard mini-batch training with batch size 512 and no learning-rate scheduler. Instead, we rely on early stopping with a patience of 10 epochs based on the validation loss. In all cases, the per-sample regression weights w_i are the same and are described in Appendix B. For the DA term, we fix the MMD loss weight to $\lambda = 0.5$ and the RBF kernel bandwidth to $\sigma = 1.0$. These values were selected on the basis of a small grid search over $\lambda \in \{0.1, 0.5, 0.9\}$ and $\sigma \in \{0.1, 1.0\}$: all combinations yielded similar regression losses, with more aggressive settings (larger λ and smaller σ) slightly lowering the total training loss but leading to more volatile training and a stronger

trade-off between domain alignment and regression accuracy. The choice $(\lambda, \sigma) = (0.5, 1.0)$ provides a stable, mid-range configuration that balances the contribution of the MMD term without pushing either hyperparameter to an extreme.

ACKNOWLEDGEMENTS

It's a pleasure to thank Taebong Jeong, Aswin Neelakandan for fruitful discussions. This work was supported by resources provided by the Pawsey Supercomputing Research Centre's Setonix Supercomputer (<https://doi.org/10.48569/18sb-8s43>) and Acacia Object Storage (<https://doi.org/10.48569/nfe9-a426>), with funding from the Australian Government and the Government of Western Australia. The authors acknowledge the Texas Advanced Computing Center (TACC) at The University of Texas at Austin for providing computational resources that have contributed to the research results reported within this paper.

This work made use of premier images captured by Subaru Telescope on the summit of Maunakea, Hawaii. We acknowledge the cultural, historical, and natural significance and reverence that Maunakea has for the indigenous Hawaiian community. We are deeply fortunate and grateful to share in the opportunity to explore the Universe from this mountain. The Hyper Suprime-Cam (HSC) collaboration includes the astronomical communities of Japan and Taiwan, and Princeton University. The HSC instrumentation and software were developed by the National Astronomical Observatory of Japan (NAOJ), the Kavli Institute for the Physics and Mathematics of the Universe (Kavli IPMU), the University of Tokyo, the High Energy Accelerator Research Organization (KEK), the Academia Sinica Institute for Astronomy and Astrophysics in Taiwan (ASIAA), and Princeton University. Funding was contributed by the FIRST program from Japanese Cabinet Office, the Ministry of Education, Culture, Sports, Science and Technology (MEXT), the Japan Society for the Promotion of Science (JSPS), Japan Science and Technology Agency (JST), the Toray Science Foundation, NAOJ, Kavli IPMU, KEK, ASIAA, and Princeton University. KGL acknowledges support from JSPS Kakenhi grant Nos. JP18H05868, JP19K14755 and JP24H00241. Kavli IPMU is supported by the World Premier International Research Center Initiative (WPI), MEXT, Japan. This work was performed in part at the Center for Data-Driven Discovery, Kavli IPMU (WPI).

REFERENCES

- Agarwal, S., Ćiprijanović, A., & Nord, B. D. 2025, Neural Network Prediction of Strong Lensing Systems with Domain Adaptation and Uncertainty Quantification, arXiv, doi: [10.48550/arXiv.2411.03334](https://doi.org/10.48550/arXiv.2411.03334)
- Aihara, H., AlSayyad, Y., Ando, M., et al. 2022, Publications of the Astronomical Society of Japan, 74, 247, doi: [10.1093/pasj/psab122](https://doi.org/10.1093/pasj/psab122)
- Albrecht, A., Bernstein, G., Cahn, R., et al. 2006, arXiv e-prints, astro, doi: [10.48550/arXiv.astro-ph/0609591](https://doi.org/10.48550/arXiv.astro-ph/0609591)
- Alsing, J., Charnock, T., Feeney, S., & Wandelt, B. 2019, Monthly Notices of the Royal Astronomical Society, stz1960, doi: [10.1093/mnras/stz1960](https://doi.org/10.1093/mnras/stz1960)
- Ayroulou, M., Nelson, D., & Pillepich, A. 2023, Monthly Notices of the Royal Astronomical Society, 524, 5391, doi: [10.1093/mnras/stad2046](https://doi.org/10.1093/mnras/stad2046)
- Baes, M., Verstacken, J., De Looze, I., et al. 2011, The Astrophysical Journal Supplement Series, 196, 22, doi: [10.1088/0067-0049/196/2/22](https://doi.org/10.1088/0067-0049/196/2/22)
- Bartelmann, M., & Maturi, M. 2016, Weak gravitational lensing, arXiv, doi: [10.48550/arXiv.1612.06535](https://doi.org/10.48550/arXiv.1612.06535)
- Beers, T. C., Flynn, K., & Gebhardt, K. 1990, The Astronomical Journal, 100, 32, doi: [10.1086/115487](https://doi.org/10.1086/115487)
- Behroozi, P., Wechsler, R. H., Hearin, A. P., & Conroy, C. 2019, MNRAS, 488, 3143, doi: [10.1093/mnras/stz1182](https://doi.org/10.1093/mnras/stz1182)
- Bottrell, C., Hani, M. H., Teimoorinia, H., et al. 2019, Monthly Notices of the Royal Astronomical Society, 490, 5390, doi: [10.1093/mnras/stz2934](https://doi.org/10.1093/mnras/stz2934)
- Bottrell, C., Yesuf, H. M., Popping, G., et al. 2024, Monthly Notices of the Royal Astronomical Society, 527, 6506, doi: [10.1093/mnras/stad2971](https://doi.org/10.1093/mnras/stad2971)
- Bruzual, G., & Charlot, S. 2003, Monthly Notices of the Royal Astronomical Society, 344, 1000, doi: [10.1046/j.1365-8711.2003.06897.x](https://doi.org/10.1046/j.1365-8711.2003.06897.x)
- Calderon, V. F., & Berlind, A. A. 2019, Monthly Notices of the Royal Astronomical Society, 490, 2367, doi: [10.1093/mnras/stz2775](https://doi.org/10.1093/mnras/stz2775)
- Camps, P., & Baes, M. 2015, Astronomy and Computing, 9, 20, doi: [10.1016/j.ascom.2014.10.004](https://doi.org/10.1016/j.ascom.2014.10.004)
- Camps, P., & Baes, M. 2020, Astronomy and Computing, 31, 100381, doi: [10.1016/j.ascom.2020.100381](https://doi.org/10.1016/j.ascom.2020.100381)
- Cannon, P., Ward, D., & Schmon, S. M. 2022, Investigating the Impact of Model Misspecification in Neural Simulation-based Inference, arXiv, doi: [10.48550/arXiv.2209.01845](https://doi.org/10.48550/arXiv.2209.01845)

- Chabrier, G. 2003, *Publications of the Astronomical Society of the Pacific*, 115, 763, doi: [10.1086/376392](https://doi.org/10.1086/376392)
- Charnock, T., Lavaux, G., & Wandelt, B. D. 2018, *Physical Review D*, 97, 083004, doi: [10.1103/PhysRevD.97.083004](https://doi.org/10.1103/PhysRevD.97.083004)
- Conselice, C. J. 2003, *The Astrophysical Journal Supplement Series*, 147, 1, doi: [10.1086/375001](https://doi.org/10.1086/375001)
- Crain, R. A., Schaye, J., Bower, R. G., et al. 2015, *Monthly Notices of the Royal Astronomical Society*, 450, 1937, doi: [10.1093/mnras/stv725](https://doi.org/10.1093/mnras/stv725)
- Cranmer, K., Brehmer, J., & Louppe, G. 2020, *Proceedings of the National Academy of Sciences*, 117, 30055, doi: [10.1073/pnas.1912789117](https://doi.org/10.1073/pnas.1912789117)
- Davé, R., Anglés-Alcázar, D., Narayanan, D., et al. 2019, *Monthly Notices of the Royal Astronomical Society*, 486, 2827, doi: [10.1093/mnras/stz937](https://doi.org/10.1093/mnras/stz937)
- Driver, S. P., Robotham, A. S. G., Obreschkow, D., et al. 2022, *Monthly Notices of the Royal Astronomical Society*, 515, 2138, doi: [10.1093/mnras/stac581](https://doi.org/10.1093/mnras/stac581)
- Eisert, L., Bottrell, C., Pillepich, A., et al. 2024, *Monthly Notices of the Royal Astronomical Society*, 528, 7411, doi: [10.1093/mnras/stae481](https://doi.org/10.1093/mnras/stae481)
- Eke, V. R., Baugh, C. M., Cole, S., et al. 2004, *Monthly Notices of the Royal Astronomical Society*, 348, 866, doi: [10.1111/j.1365-2966.2004.07408.x](https://doi.org/10.1111/j.1365-2966.2004.07408.x)
- Farahani, A., Voghoei, S., Rasheed, K., & Arabnia, H. R. 2020, *A Brief Review of Domain Adaptation*, arXiv, doi: [10.48550/arXiv.2010.03978](https://doi.org/10.48550/arXiv.2010.03978)
- Ganin, Y., Ustinova, E., Ajakan, H., et al. 2017, in *Domain Adaptation in Computer Vision Applications*, ed. G. Csurka (Cham: Springer International Publishing), 189–209, doi: [10.1007/978-3-319-58347-1_10](https://doi.org/10.1007/978-3-319-58347-1_10)
- Garuda, N., Wu, J. F., Nelson, D., & Pillepich, A. 2024, *Estimating Dark Matter Halo Masses in Simulated Galaxy Clusters with Graph Neural Networks*, arXiv, doi: [10.48550/arXiv.2411.12629](https://doi.org/10.48550/arXiv.2411.12629)
- Greenberg, D. S., Nonnenmacher, M., & Macke, J. H. 2019, *Automatic Posterior Transformation for Likelihood-Free Inference*, arXiv, doi: [10.48550/arXiv.1905.07488](https://doi.org/10.48550/arXiv.1905.07488)
- Gretton, A., Borgwardt, K., Rasch, M. J., Scholkopf, B., & Smola, A. J. 2008, *A Kernel Method for the Two-Sample Problem*, arXiv, doi: [10.48550/ARXIV.0805.2368](https://doi.org/10.48550/ARXIV.0805.2368)
- Groves, B., Dopita, M. A., Sutherland, R. S., et al. 2008, *The Astrophysical Journal Supplement Series*, 176, 438, doi: [10.1086/528711](https://doi.org/10.1086/528711)
- Hahn, C., Bottrell, C., & Lee, K.-G. 2024, *The Astrophysical Journal*, 968, 90, doi: [10.3847/1538-4357/ad4344](https://doi.org/10.3847/1538-4357/ad4344)
- Hahn, C., Eickenberg, M., Ho, S., et al. 2023, *Proceedings of the National Academy of Sciences*, 120, e2218810120, doi: [10.1073/pnas.2218810120](https://doi.org/10.1073/pnas.2218810120)
- Handley, W., & Millea, M. 2019, *Entropy*, 21, 272, doi: [10.3390/e21030272](https://doi.org/10.3390/e21030272)
- Hearin, A. P., Zentner, A. R., Berlind, A. A., & Newman, J. A. 2013, *Monthly Notices of the Royal Astronomical Society*, 433, 659, doi: [10.1093/mnras/stt755](https://doi.org/10.1093/mnras/stt755)
- Heisler, J., Tremaine, S., & Bahcall, J. N. 1985, *The Astrophysical Journal*, 298, 8, doi: [10.1086/163584](https://doi.org/10.1086/163584)
- Hoekstra, H., Bartelmann, M., Dahle, H., et al. 2013, *Space Science Reviews*, 177, 75, doi: [10.1007/s11214-013-9978-5](https://doi.org/10.1007/s11214-013-9978-5)
- Hopkins, P. F. 2015, *Monthly Notices of the Royal Astronomical Society*, 450, 53, doi: [10.1093/mnras/stv195](https://doi.org/10.1093/mnras/stv195)
- Hopkins, P. F. 2017, *A New Public Release of the GIZMO Code*, arXiv, doi: [10.48550/arXiv.1712.01294](https://doi.org/10.48550/arXiv.1712.01294)
- Huang, D., Bharti, A., Souza, A., Acerbi, L., & Kaski, S. 2023, *Learning Robust Statistics for Simulation-based Inference under Model Misspecification*, arXiv, doi: [10.48550/arXiv.2305.15871](https://doi.org/10.48550/arXiv.2305.15871)
- Jeffrey, N., & Wandelt, B. D. 2020, arXiv e-prints, arXiv:2011.05991, doi: [10.48550/arXiv.2011.05991](https://doi.org/10.48550/arXiv.2011.05991)
- Kawanomoto, S., Uraguchi, F., Komiyama, Y., et al. 2018, *Publications of the Astronomical Society of Japan*, 70, doi: [10.1093/pasj/psy056](https://doi.org/10.1093/pasj/psy056)
- Kouw, W. M., & Loog, M. 2019, *An introduction to domain adaptation and transfer learning*, arXiv, doi: [10.48550/arXiv.1812.11806](https://doi.org/10.48550/arXiv.1812.11806)
- Kravtsov, A. V., Berlind, A. A., Wechsler, R. H., et al. 2004, *The Astrophysical Journal*, 609, 35, doi: [10.1086/420959](https://doi.org/10.1086/420959)
- Lakshminarayanan, B., Pritzel, A., & Blundell, C. 2019, in *CANCER METASTASIS LEE19-01474* (arXiv), doi: [10.3389/978-2-88963-094-3](https://doi.org/10.3389/978-2-88963-094-3)
- Lambert, T. S., Robotham, A. S. G., Bravo, M., et al. 2026, *Astronomy and Computing*, 54, 101011, doi: [10.1016/j.ascom.2025.101011](https://doi.org/10.1016/j.ascom.2025.101011)
- Lee, K.-G., Ata, M., Khrykin, I. S., et al. 2022, *The Astrophysical Journal*, 928, 9, doi: [10.3847/1538-4357/ac4f62](https://doi.org/10.3847/1538-4357/ac4f62)
- Lee, K.-G., Khrykin, I. S., Simha, S., et al. 2023, *ApJL*, 954, L7, doi: [10.3847/2041-8213/acefb5](https://doi.org/10.3847/2041-8213/acefb5)
- Lemos, P., Coogan, A., Hezaveh, Y., & Perreault-Levasseur, L. 2023, in *Proceedings of the 40th International Conference on Machine Learning (PMLR)*, 19256–19273. <https://proceedings.mlr.press/v202/lemos23a.html>
- Li, S.-S., Hoekstra, H., Kuijken, K., Schaller, M., & Schaye, J. 2025, *Astronomy & Astrophysics*, 700, A202, doi: [10.1051/0004-6361/202452892](https://doi.org/10.1051/0004-6361/202452892)
- Loshchilov, I., & Hutter, F. 2019, *Decoupled Weight Decay Regularization*, arXiv, doi: [10.48550/arXiv.1711.05101](https://doi.org/10.48550/arXiv.1711.05101)
- Lotz, J. M., Primack, J., & Madau, P. 2004, *The Astronomical Journal*, 128, 163, doi: [10.1086/421849](https://doi.org/10.1086/421849)

- Lucas Makinen, T., Heavens, A., Porqueres, N., et al. 2025, *Journal of Cosmology and Astroparticle Physics*, 2025, 095, doi: [10.1088/1475-7516/2025/01/095](https://doi.org/10.1088/1475-7516/2025/01/095)
- Makinen, T. L., Charnock, T., Alsing, J., & Wandelt, B. D. 2021, *Journal of Cosmology and Astroparticle Physics*, 2021, 049, doi: [10.1088/1475-7516/2021/11/049](https://doi.org/10.1088/1475-7516/2021/11/049)
- Mandelbaum, R. 2018, *Annual Review of Astronomy and Astrophysics*, 56, 393, doi: [10.1146/annurev-astro-081817-051928](https://doi.org/10.1146/annurev-astro-081817-051928)
- Marinacci, F., Vogelsberger, M., Pakmor, R., et al. 2018, *Monthly Notices of the Royal Astronomical Society*, doi: [10.1093/mnras/sty2206](https://doi.org/10.1093/mnras/sty2206)
- McInnes, L., Healy, J., & Melville, J. 2020, UMAP: Uniform Manifold Approximation and Projection for Dimension Reduction, arXiv, doi: [10.48550/arXiv.1802.03426](https://doi.org/10.48550/arXiv.1802.03426)
- Montel, N. A., Alvey, J., & Weniger, C. 2025, Tests for model misspecification in simulation-based inference: from local distortions to global model checks, arXiv, doi: [10.48550/arXiv.2412.15100](https://doi.org/10.48550/arXiv.2412.15100)
- Moster, B. P., Naab, T., & White, S. D. M. 2013, *Monthly Notices of the Royal Astronomical Society*, 428, 3121, doi: [10.1093/mnras/sts261](https://doi.org/10.1093/mnras/sts261)
- Naiman, J. P., Pillepich, A., Springel, V., et al. 2018, *Monthly Notices of the Royal Astronomical Society*, 477, 1206, doi: [10.1093/mnras/sty618](https://doi.org/10.1093/mnras/sty618)
- Natarajan, P., Williams, L. L. R., Bradač, M., et al. 2024, *Space Science Reviews*, 220, 19, doi: [10.1007/s11214-024-01051-8](https://doi.org/10.1007/s11214-024-01051-8)
- Nelson, D., Pillepich, A., Springel, V., et al. 2018, *Monthly Notices of the Royal Astronomical Society*, 475, 624, doi: [10.1093/mnras/stx3040](https://doi.org/10.1093/mnras/stx3040)
- Nelson, D., Springel, V., Pillepich, A., et al. 2019a, *Computational Astrophysics and Cosmology*, 6, 2, doi: [10.1186/s40668-019-0028-x](https://doi.org/10.1186/s40668-019-0028-x)
- Nelson, D., Pillepich, A., Springel, V., et al. 2019b, *Monthly Notices of the Royal Astronomical Society*, 490, 3234, doi: [10.1093/mnras/stz2306](https://doi.org/10.1093/mnras/stz2306)
- Ntampaka, M., Trac, H., Sutherland, D. J., et al. 2015, *The Astrophysical Journal*, 803, 50, doi: [10.1088/0004-637X/803/2/50](https://doi.org/10.1088/0004-637X/803/2/50)
- Ntampaka, M., Trac, H., Sutherland, D. J., et al. 2016, *The Astrophysical Journal*, 831, 135, doi: [10.3847/0004-637X/831/2/135](https://doi.org/10.3847/0004-637X/831/2/135)
- Papamakarios, G., & Murray, I. 2018, Fast ϵ -free Inference of Simulation Models with Bayesian Conditional Density Estimation, arXiv, doi: [10.48550/arXiv.1605.06376](https://doi.org/10.48550/arXiv.1605.06376)
- Papamakarios, G., Pavlakou, T., & Murray, I. 2018, Masked Autoregressive Flow for Density Estimation, arXiv, doi: [10.48550/arXiv.1705.07057](https://doi.org/10.48550/arXiv.1705.07057)
- Parul, H., Gleyzer, S., Reddy, P., & Toomey, M. W. 2025, *The Astrophysical Journal*, 990, 47, doi: [10.3847/1538-4357/adee16](https://doi.org/10.3847/1538-4357/adee16)
- Pillepich, A., Nelson, D., Hernquist, L., et al. 2018, *Monthly Notices of the Royal Astronomical Society*, 475, 648, doi: [10.1093/mnras/stx3112](https://doi.org/10.1093/mnras/stx3112)
- Pillepich, A., Nelson, D., Springel, V., et al. 2019, *Monthly Notices of the Royal Astronomical Society*, 490, 3196, doi: [10.1093/mnras/stz2338](https://doi.org/10.1093/mnras/stz2338)
- Popping, G., Pillepich, A., Calistro Rivera, G., et al. 2022, *Monthly Notices of the Royal Astronomical Society*, 510, 3321, doi: [10.1093/mnras/stab3312](https://doi.org/10.1093/mnras/stab3312)
- Putter, R. d., & White, M. 2005, *New Astronomy*, 10, 676, doi: [10.1016/j.newast.2005.05.001](https://doi.org/10.1016/j.newast.2005.05.001)
- Rana, D., More, S., Miyatake, H., et al. 2022, *Monthly Notices of the Royal Astronomical Society*, 510, 5408, doi: [10.1093/mnras/stac007](https://doi.org/10.1093/mnras/stac007)
- Robotham, A. S. G., Bellstedt, S., & Driver, S. P. 2022, *Monthly Notices of the Royal Astronomical Society*, 513, 2985, doi: [10.1093/mnras/stac1032](https://doi.org/10.1093/mnras/stac1032)
- Robotham, A. S. G., Davies, L. J. M., Driver, S. P., et al. 2018, *Monthly Notices of the Royal Astronomical Society*, 476, 3137, doi: [10.1093/mnras/sty440](https://doi.org/10.1093/mnras/sty440)
- Robotham, A. S. G., Taranu, D. S., Tobar, R., Moffett, A., & Driver, S. P. 2017, *Monthly Notices of the Royal Astronomical Society*, 466, 1513, doi: [10.1093/mnras/stw3039](https://doi.org/10.1093/mnras/stw3039)
- Robotham, A. S. G., Norberg, P., Driver, S. P., et al. 2011, *Monthly Notices of the Royal Astronomical Society*, 416, 2640, doi: [10.1111/j.1365-2966.2011.19217.x](https://doi.org/10.1111/j.1365-2966.2011.19217.x)
- Roncoli, A., Čiprijanović, A., Voetberg, M., Villaescusa-Navarro, F., & Nord, B. 2024, Domain Adaptive Graph Neural Networks for Constraining Cosmological Parameters Across Multiple Data Sets, arXiv, doi: [10.48550/arXiv.2311.01588](https://doi.org/10.48550/arXiv.2311.01588)
- Rémy-Ruyer, A., Madden, S. C., Galliano, F., et al. 2014, *Astronomy & Astrophysics*, 563, A31, doi: [10.1051/0004-6361/201322803](https://doi.org/10.1051/0004-6361/201322803)
- Schaller, M., Dalla Vecchia, C., Schaye, J., et al. 2015, *Monthly Notices of the Royal Astronomical Society*, 454, 2277, doi: [10.1093/mnras/stv2169](https://doi.org/10.1093/mnras/stv2169)
- Schaye, J., Crain, R. A., Bower, R. G., et al. 2015, *Monthly Notices of the Royal Astronomical Society*, 446, 521, doi: [10.1093/mnras/stu2058](https://doi.org/10.1093/mnras/stu2058)
- Shajib, A. J., Vernardos, G., Collett, T. E., et al. 2024, *Space Science Reviews*, 220, 87, doi: [10.1007/s11214-024-01105-x](https://doi.org/10.1007/s11214-024-01105-x)
- Sicilia, A., Zhao, X., & Hwang, S. J. 2023, *Machine Learning*, 112, 2685, doi: [10.1007/s10994-023-06324-x](https://doi.org/10.1007/s10994-023-06324-x)

- Simard, L., Mendel, J. T., Patton, D. R., Ellison, S. L., & McConnachie, A. W. 2011, *The Astrophysical Journal Supplement Series*, 196, 11, doi: [10.1088/0067-0049/196/1/11](https://doi.org/10.1088/0067-0049/196/1/11)
- Springel, V. 2010, *Monthly Notices of the Royal Astronomical Society*, 401, 791, doi: [10.1111/j.1365-2966.2009.15715.x](https://doi.org/10.1111/j.1365-2966.2009.15715.x)
- Springel, V., White, S. D. M., Tormen, G., & Kauffmann, G. 2001, *Monthly Notices of the Royal Astronomical Society*, 328, 726, doi: [10.1046/j.1365-8711.2001.04912.x](https://doi.org/10.1046/j.1365-8711.2001.04912.x)
- Springel, V., Pakmor, R., Pillepich, A., et al. 2018, *Monthly Notices of the Royal Astronomical Society*, 475, 676, doi: [10.1093/mnras/stx3304](https://doi.org/10.1093/mnras/stx3304)
- Sullivan, A., Power, C., Bottrell, C., Robotham, A., & Shabala, S. 2024, *Publications of the Astronomical Society of Australia*, 41, e022, doi: [10.1017/pasa.2024.24](https://doi.org/10.1017/pasa.2024.24)
- Swierc, P., Zhao, M., Ćiprijanović, A., & Nord, B. 2023, *Domain Adaptation for Measurements of Strong Gravitational Lenses*, arXiv, doi: [10.48550/arXiv.2311.17238](https://doi.org/10.48550/arXiv.2311.17238)
- Tabak, E. G., & Turner, C. V. 2013, *Communications on Pure and Applied Mathematics*, 66, 145, doi: [10.1002/cpa.21423](https://doi.org/10.1002/cpa.21423)
- Tabak, E. G., & Vanden-Eijnden, E. 2010, *Communications in Mathematical Sciences*, 8, 217, doi: [10.4310/CMS.2010.v8.n1.a11](https://doi.org/10.4310/CMS.2010.v8.n1.a11)
- Tasitsiomi, A., Kravtsov, A. V., Wechsler, R. H., & Primack, J. R. 2004, *The Astrophysical Journal*, 614, 533, doi: [10.1086/423784](https://doi.org/10.1086/423784)
- Tinker, J., Wetzel, A., & Conroy, C. 2011, *Are Halo and Galaxy Formation Histories Correlated?* arXiv, doi: [10.48550/arXiv.1107.5046](https://doi.org/10.48550/arXiv.1107.5046)
- Tinker, J. L. 2022, *The Astronomical Journal*, 163, 126, doi: [10.3847/1538-3881/ac37bb](https://doi.org/10.3847/1538-3881/ac37bb)
- Treu, T. 2010, *Annual Review of Astronomy and Astrophysics*, 48, 87, doi: [10.1146/annurev-astro-081309-130924](https://doi.org/10.1146/annurev-astro-081309-130924)
- Vale, A., & Ostriker, J. P. 2004, *Monthly Notices of the Royal Astronomical Society*, 353, 189, doi: [10.1111/j.1365-2966.2004.08059.x](https://doi.org/10.1111/j.1365-2966.2004.08059.x)
- Vilalta, R., Gupta, K. D., Boumber, D., & Meskhi, M. M. 2019, *Publications of the Astronomical Society of the Pacific*, 131, 108008, doi: [10.1088/1538-3873/aaf1fc](https://doi.org/10.1088/1538-3873/aaf1fc)
- Villanueva-Domingo, P., Villaescusa-Navarro, F., Anglés-Alcázar, D., et al. 2022, *The Astrophysical Journal*, 935, 30, doi: [10.3847/1538-4357/ac7aa3](https://doi.org/10.3847/1538-4357/ac7aa3)
- Wechsler, R. H., & Tinker, J. L. 2018, *ARA&A*, 56, 435, doi: [10.1146/annurev-astro-081817-051756](https://doi.org/10.1146/annurev-astro-081817-051756)
- Wojtak, R., Old, L., Mamon, G. A., et al. 2018, *Monthly Notices of the Royal Astronomical Society*, 481, 324, doi: [10.1093/mnras/sty2257](https://doi.org/10.1093/mnras/sty2257)
- Wright, R. J., Somerville, R. S., Lagos, C. d. P., et al. 2024, *Monthly Notices of the Royal Astronomical Society*, 532, 3417, doi: [10.1093/mnras/stae1688](https://doi.org/10.1093/mnras/stae1688)
- Wu, J. F., Jespersen, C. K., & Wechsler, R. H. 2024, *The Astrophysical Journal*, 976, 37, doi: [10.3847/1538-4357/ad7bb3](https://doi.org/10.3847/1538-4357/ad7bb3)
- Yang, X., Mo, H. J., Bosch, F. C. v. d., et al. 2007, *The Astrophysical Journal*, 671, 153, doi: [10.1086/522027](https://doi.org/10.1086/522027)
- Yang, X., Mo, H. J., & Van Den Bosch, F. C. 2009, *The Astrophysical Journal*, 695, 900, doi: [10.1088/0004-637X/695/2/900](https://doi.org/10.1088/0004-637X/695/2/900)
- Yang, X., Mo, H. J., van den Bosch, F. C., et al. 2006, *Monthly Notices of the Royal Astronomical Society*, 373, 1159, doi: [10.1111/j.1365-2966.2006.11091.x](https://doi.org/10.1111/j.1365-2966.2006.11091.x)
- Zaritsky, D., & Behroozi, P. 2022, *Monthly Notices of the Royal Astronomical Society*, 519, 871, doi: [10.1093/mnras/stac3610](https://doi.org/10.1093/mnras/stac3610)
- Zhao, H., Des Combes, R. T., Zhang, K., & Gordon, G. 2019, in *International conference on machine learning (PMLR)*, 7523–7532
- Ćiprijanović, A., Lewis, A., Pedro, K., et al. 2023, *Machine Learning: Science and Technology*, 4, 025013, doi: [10.1088/2632-2153/acca5f](https://doi.org/10.1088/2632-2153/acca5f)
- Ćiprijanović, A., Kafkes, D., Snyder, G., et al. 2022, *Machine Learning: Science and Technology*, 3, 035007, doi: [10.1088/2632-2153/ac7f1a](https://doi.org/10.1088/2632-2153/ac7f1a)